Comparative analysis of the performance of the GOFS, PSY4 and AMSEAS ocean model frameworks in the Virgin Islands and Puerto Rico coastal ocean

Sonaljit Mukherjee *1, Sennai Habtes †1, and Paul Jobsis ‡1

[1]Center for Marine and Environmental Studies, University of the Virgin Islands

Abstract

This work compares the performance of 3 ocean model frameworks that currently produce outputs of the ocean properties specific to the US Caribbean ocean; the Global Ocean Forecast System (GOFS), US Navy Coastal Ocean Model for the American Seas (AMSEAS), and the Daily Global Physical Bulletin (PSY4). Separate comparisons are done for the ocean properties in the open ocean and the nearshore regions. For the open ocean, the model outputs are compared with the AVISO satellite altimetry data for the sea-surface height anomaly (SSHA), the OSCAR data for surface current velocities, and the G1SST satellite data for sea-surface temperature (SST). For the nearshore analysis, the model outputs are compared with in-situ buoy measurements and HOBO logger data in the nearshore regions. Our analysis shows that the PSY4 produces the most realistic outputs of SSHA and surface current velocities in the open ocean, whereas all the models produce a strong correlation in terms of the seasonal variability of the surface temperature when compared to the G1SST data. The AMSEAS model, despite being a fine resolution regional model, under-performs in terms of the surface current velocity outputs in the open ocean due to the influence of the simulated submesoscale turbulence on the mesoscale variability. In the nearshore regions, none of the models produce agreeable outputs on the SSHA and current velocities. These findings provide useful insight on the applicability of the model outputs for various operations that require oceanographic data specific to the US Caribbean ocean.

1 Introduction

The coastal ocean surrounding the US Virgin Islands (VI) and Puerto Rico (PR) boasts vibrant marine ecosystems. Many of the drivers regulating the ecological processes in the coastal ecosystems of the region are strongly influenced by the physical and thermodynamic variables of the surrounding coastal waters. For example, larval transport in the coastal ocean is influenced by large-scale processes like O(100 km) mesoscale eddies, as well as small-scale processes like surface gravity waves, buoyancy-driven flows, atmospheric fluxes and both surface and internal tides [Pineda et al., 2007]. Furthermore, the resilience of coral reef ecosystems can be impacted by a variety of factors like the seasonal variability of benthic temperature, the sedimentation rate and mechanical stress produced by surface waves [Pineda et al., 2007]. A necessary step towards understanding the factors that facilitate or hamper the health and resilience of coastal ecosystems, is to have realistic estimates of

*sonaljit.mukherjee@uvi.edu
†shabtes@gmail.com
‡pjobsis@uvi.edu

the circulation and thermodynamic characteristics of the surrounding ocean. Due to the complexity of the instrumentation involved in obtaining 3-dimensional (3D) gridded data on the physical and thermodynamic properties of the ocean, characterizing the ocean state and circulation is done using computational ocean models coupled with data assimilation algorithms.

A numerical ocean circulation model with finite difference algorithm uses numerically discretized prognostic equations that advance the momentum and scalar variables with respect to time. The grid resolution of a numerical ocean model limits the dimension of the smallest circulation features that a model can resolve. For example, a horizontal resolution of 1 km permits the model to represent eddies with a minimum diameter of roughly 10 km. The inability to resolve turbulent fluxes at scales lower than the permitted scale based on the grid resolution, creates a bias in the simulated ocean properties. This bias accumulates over time, producing unrealistic outputs of the momentum and scalar fields. This problem is partially mitigated by constraining and adjusting the model outputs towards the observed ocean properties using data assimilation [Marchesiello et al., 2001, Hoteit et al., 2018]. Such a combined framework of ocean models and data assimilation algorithms had been successfully used to hindcast ocean circulation and scalar variability at various coastal and open ocean regions [Chassignet et al., 2007, Rowley and Mask, 2014]. Notable forecast systems in operation include the Global Ocean Forecast System (GOFS), the Relocatable nowcast/forecast system (RELO), the Global Ocean Physical Analysis at $1/12^0$ (PSY4) by Mercator Ocean, Bluelink by the Commonwealth Scientific and Industrial Research Organization (CSIRO) for Australia, Forecasting Ocean Assimilation Model (FOAM) for the UK, and the Topaz Monitoring system for Norway [Hernandez et al., 2009, Madec, 2008, Rowley and Mask, 2014, Oke et al., 2008, Storkey et al., 2010]. Each modeling framework implements a unique set of parameters including but not limited to the vertical grid structure, advection and diffusion algorithms, grid resolution and subgrid mixing parameterizations. Depending on the region of interest, these models use locally available observed data for assimilation and the surface flux outputs from atmospheric models to produce 3D gridded outputs of the ocean state and circulation.

As part of an international research initiative by the Global Ocean Data Assimilation Experiment (GODAE), a comparative analysis between the different ocean forecasting systems have revealed the strengths and weaknesses of the different modeling frameworks. These strengths and weaknesses vary based on the model parameters, data used for assimilation, and the region of interest. These comparative studies, conducted in the Tasman and Coral seas and along the east coast of Australia, indicate that the Bluelink (CSIRO) provides the most realistic sea-surface height (SSH) variability, whereas FOAM (UK) provides the most realistic subsurface temperature and salinity specific to the Tasman and Coral Sea region [Oke et al., 2012].

For our region of interest, which is the US Caribbean ocean surrounding Puerto Rico (PR) and the Virgin Islands (VI), there is currently no operational regional ocean modeling framework available to aid to our ongoing marine research. Our long-term goal is to develop a coastal regional ocean forecasting system for the US Caribbean ocean capable of resolving the flow around the relatively small islands in the region with a sufficiently fine resolution that permits O(1 km) submesoscale eddies over a domain large enough to permit the modeling of O(100 km) mesoscale eddies. As an example, the blue rectangle in figure 1 depicts a typical domain for the proposed regional ocean model for the US Caribbean ocean containing PR and the VI. Such a regional model will require 3D gridded open-ocean data on the temperature, salinity and current velocities as boundary conditions. Since the 3D gridded observational data in the open ocean is impossible to obtain due to complexities of the instrumentation involved, we have to rely on the available coarse resolution model frameworks that produce simulated 3D outputs of the ocean properties in the open-ocean surrounding the islands. Therefore, it is necessary to compare the gridded outputs from existing model frameworks with the available observational datasets for PR and the VI and to determine the strengths and weaknesses of each model framework.

In this work, we do a comparative analysis of the performance of 3 ocean model frameworks that provide 3D gridded data for the coastal ocean surrounding the VI and PR; the Global Ocean Forecasting System (GOFS), the Navy Coastal Ocean Model for American Seas (AMSEAS), and the Global Ocean Physical Analysis at $1/12^0$ (PSY4) by Mercator Ocean [Hernandez et al., 2009, Madec, 2008, Rowley and Mask, 2014]. While the PSY4 and GOFS are global ocean forecasting systems at a resolution of 10 km, the AMSEAS is a regional ocean forecasting system that operates 3 separate grids for the Alaskan seas, the US East, and the American Seas (AMSEAS) covering the Gulf of Mexico and the Caribbean Sea at a resolution of 3 km. For assimilating observed data, both the GOFS and the AMSEAS regional system use the NCODA [Cummings and Smedstad, 2013], whereas the PSY4 uses the SEEK filter [Brasseur and Verron, 2006].

We evaluate the performance of these model frameworks by comparing their outputs with available observational data on the sea-surface height anomaly (SSHA), surface current velocities, seasonal variability of the sea-surface temperature (SST) and the in-situ benthic temperature. Section 2 provides a brief overview of the circulation in the Caribbean Sea with a particular focus on the coastal circulation of the US Caribbean. Section 3 provides a brief overview of the currently available model frameworks for the islands in the region, namely the PSY4, GOFS and the AMSEAS. Section 4 provides an overview of the available observational data and the nearshore ocean properties for the US Caribbean. In section 5, we explain the different metrics and analyses used to evaluate the model performance by comparing simulated outputs with the observed data mentioned above. Section 6 discusses the results from the analysis of model performance and section 7 summarizes our conclusions regarding which circulation model frameworks are appropriate for use in the US Caribbean ocean.

2 Ocean Circulation Surrounding Puerto Rico and the Virgin Islands

Puerto Rico and the Virgin Islands lie along the northern arc of the Antilles islands, a group of islands bordering the northeastern rim of the Caribbean Sea (figure 1). The ocean circulation surrounding these islands is largely influenced by the westward inflow of the Atlantic gyre circulation into the Caribbean Sea through the passages between the islands of the lesser Antilles. The Caribbean Current, spanning the southern portion of the Caribbean Sea between latitudes 13^0 and 16^0 N, is largely driven by the inflow of the Atlantic Meridional Overturning Circulation (AMOC) through the Windward and Leeward island passages [Johns et al., 2002]. This inflow of the AMOC forms approximately two-thirds of the net inflow from the Atlantic Ocean into the Caribbean Sea. The remaining one-third of the inflow occurs between the passages of the islands in the Greater Antilles; the Anegada-Jungfern passage complex to the east separating the Virgin Islands from the Lesser Antilles beginning with Anguilla and St. Maarten, and the Mona passage to the west between Puerto Rico and Hispaniola [Johns et al., 2002]. The Anegada passage facilitates the flow of mid-depth Atlantic water into the Virgin Islands basin, and the Jungfern passage allows the flow of the Atlantic water into the Caribbean Sea [Fratantoni et al., 1997]. The strength of the Caribbean current is geostrophically enhanced by the intensification of the north-south density gradient due to the freshwater flux from the Orinoco and Amazon rivers [Chérubin and Richardson, 2007]. This freshwater plume can move northwestward through the Caribbean Sea at times reaching the southern coastline of St. Croix of the VI, creating turbulent wakes in the offshore region of the northeastern coast of St Croix [Chérubin and Garavelli, 2016]. The flow along the northern coastline of the Greater Antilles islands has been characterized as a discontinuous eddy field that transports warm water northwestward as it merges with the Florida current [Gunn and Watts, 1982]. Simulating the complexity of these features is beyond the capability of the currently operational global ocean models due to coarse resolutions. Therefore, it is necessary to develop a downscaled ocean circulation model with a resolution less than 1 km to realistically simulate the small-scale features and their impact on the mesoscale circulation.

3 Ocean Model Frameworks

Currently, the model frameworks that provide simulated outputs of the coastal ocean circulation around PR and the VI are the GOFS [Hernandez et al., 2009], the AMSEAS [Rowley and Mask, 2014] and the PSY4 [Madec, 2008]. Details on the parameters of these model frameworks are provided in table 1.

3.1 GOFS

The Global Ocean Forecast System (GOFS[1]), created as part of the Global Ocean Data Assimilation Experiment (GODAE) [Hernandez et al., 2009], uses the Hybrid Coordinate Ocean Model (HYCOM) [Chassignet et al., 2007]. The HYCOM is a primitive equation general circulation model using a vertical coordinate system that shifts from isopycnal coordinates in the stratified open ocean to terrain-following coordinates in the shallow coastal regions and z-level coordinates in the upper ocean boundary layer [Chassignet et al., 2007]. The horizontal discretization in GOFS is based on an orthogonal curvilinear coordinate system with a horizontal grid resolution of $1/12^0$. The surface forcing used by GOFS is obtained from the Navy Global Environmental Model (NAVGEM) [Whitcomb, 2012]. There is no tidal forcing implemented in the GOFS model framework. Detailed specifics on the GOFS system are provided in table 1.

The absence of realistic turbulent fluxes that occur at scales smaller than the grid resolution of an ocean model, results in a bias in the simulated ocean properties from the model outputs. To mitigate this bias, observed data are assimilated into the model outputs using various data assimilation techniques. The GOFS uses the Navy Coupled Ocean Data Assimilation (NCODA), a 3D multivariate optimum interpolation scheme [Cummings and Smedstad, 2013] that assimilates all quality-controlled observational data including satellite SST, altimetry derived SSHA, microwave-derived sea ice concentration, in-situ temperature and salinity measurements from ships, drifters, buoys, profiling floats, XBTs (Expendable Bathythermographs), CTDs (Conductivity, Temperature and Depth Sensors) and gliders. The NCODA version 3.1 generates subsurface temperature and salinity fields from the SST and SSHA using an Improved Ocean Synthetic Profile (ISOP) technique [Helber et al., 2013], and assimilates the subsurface fields into the model outputs using 3D Variational Data Assimilation (3DVAR, Barker et al. [2004]). The NCODA is tuned to process the observed data and constrain the model outputs towards the observed data on the order of spatial scales equivalent to or larger than the O(100 km) mesoscale [Carrier et al., 2019].

The GOFS provides 3-hourly instantaneous outputs on the momentum and scalar properties of the global oceans. In our analysis, we use the previously simulated hindcast outputs from the GOFS model in the Northern Caribbean sea, averaged over 1 day. The outputs can be obtained from the HYCOM server.

3.2 PSY4

The Daily Global Physical Bulletin at $1/12^0$ (PSY4[2]), maintained by the non-profit company Mercator Ocean, uses version 3.1 of the NEMO (Nucleus for European Modeling of the Ocean) [Madec, 2008]. The NEMO uses a tripolar ORCA grid [Madec and Imbard, 1996] with a horizontal resolution of $1/12^0$. The vertical coordinate is discretized into 50 levels with resolution increasing from 1 m near the surface to 450 m at the bottom. The PSY4 uses atmospheric forcing provided by the European Center for Medium Range Weather Forecasts (ECMWF) with a sampling time of 3 hours, and does not use any tidal forcing. For the data assimilation, the PSY4 uses the SEEK filter, which is a reduced-

[1] https://tds.hycom.org/thredds/catalog.html
[2] https://marine.copernicus.eu/

order Kalman filter with a 3D multivariate modal decomposition of the background error and a 7-day assimilation cycle [Brasseur and Verron, 2006].

The PSY4 provides hourly hindcast data on the momentum and scalar properties of the global oceans. We use the daily averaged hindcast outputs from the PSY4 in the Northern Caribbean Sea, which can be accessed from the Copernicus Marine Service server.

3.3 AMSEAS

The Relocatable ocean nowcast/forecast system [Rowley and Mask, 2014], operated by the Naval Oceanographic Office (NAVOCEANO), uses the Navy Coastal Ocean Model (NCOM[3]) at a horizontal resolution of $1/36^0$, along with the NCODA system for data assimilation. The NCOM is a primitive equation baroclinic, hydrostatic, Boussinesq ocean model with a free surface [Barron et al., 2006]. It uses an orthogonal curvilinear grid for horizontal discretization. The vertical grid used by RELO consists of a number of terrain following σ coordinate levels from the surface, and Cartesian z-levels below (table 1). The NCOM is used for regional simulation within the Alaskan domain covering the Gulf of Alaska and the Northeast Pacific, the US east coast (USEAST) and the American seas (AMSEAS) spanning the Gulf of Mexico and the Caribbean Sea (figure 2). The NCOM AMSEAS uses the 15 km application of the Navy Coupled Ocean/Atmoshpere Mesoscale Prediction System (COAMPS) for surface forcing [Hodur, 1997], and the GOFS model outputs at $1/12^0$ resolution [Chassignet et al., 2007, 2009] for boundary conditions. Tidal forcing in the NCOM AMSEAS regional setup is provided by the OTIS tidal package [Egbert and Erofeeva, 2002].

While the GOFS and PSY4 are global ocean forecast models, the NCOM AMSEAS is a regional model setup that uses the GOFS model outputs as boundary conditions and the NCODA for assimilating the observed data. The AMSEAS provides 3-hourly instantaneous outputs on the momentum and scalar properties in the Caribbean sea. In our analysis, we use the previously simulated oceanographic outputs by the AMSEAS model in the US Caribbean ocean, averaged over 1 day. The AMSEAS outputs are available on the NOAA NCOM server.

4 Observed Data

Gridded observed data available for the physical and thermodynamic properties of the Caribbean Sea are the sea-surface height anomaly (SSHA) produced by Archiving, Validation and Interpretation of Satellite Oceanographic data (AVISO, AVISO-Altimetry [1996], [Guerrero et al., 2004]), sea-surface temperature (SST) from the Group for High Resolution Sea Surface Temperature (G1SST, section 4.3), and surface current velocity estimates from the Ocean Surface Current Analysis Real-time (OSCAR, Bonjean and Lagerloef [2002], Johnson et al. [2007]).

4.1 AVISO

AVISO provides gridded satellite altimetry data products including SSHA and geostrophic velocities at a spatial resolution of $1/4^0$ of latitude, and a temporal resolution of 1 day. The AVISO SSHA data is prepared by merging the altimetry measurements from altimeters aboard the TOPEX/Poseidon, Envisat, Jason-1 and OSTM/Jason-2, satellite platforms and estimated with respect to a 20-year average [Blanc et al., 1996, Guerrero et al., 2004]. In the open ocean, away from the influence of shallow coastal bathymetry, the SSHA variability is governed by wind-driven circulation, atmospheric pressure and internal density gradients. Hence, the SSHA variability in the open ocean is an important source of information for deducing the subsurface ocean characteristics. Detailed specifics of the AVISO data are provided in table 2.

[3]https://www.ncei.noaa.gov/products/weather-climate-models/fnmoc-regional-navy-coastal-ocean

4.2 OSCAR

OSCAR is a NASA funded research project that provides surface current velocities averaged over the top 30 m of the ocean and is available at 5-day intervals. The OSCAR surface current data is developed by interpolation and analysis of SSHA, surface wind velocity and SST data obtained from satellite and in-situ measurements. The governing equations used to compute these velocities are based on a quasi-linear and quasi-steady approach with geostrophic balance, Ekman–Stommel shear dynamics and a complimentary term from the surface buoyancy gradient [Bonjean and Lagerloef, 2002, Johnson et al., 2007]. The OSCAR data is available with a horizontal resolution of $1/3^0$ and averaged over 5 days. The OSCAR provides reasonable estimates of the surface current velocities in the tropical open ocean [Sikhakolli et al., 2013]. Detailed specifics on the OSCAR dataset are provided in table 2.

4.3 G1SST

The Global 1 km Sea Surface Temperature Analysis (G1SST), maintained by the Group for High Resolution Sea Surface Temperature (GHRSST), uses satellite and in-situ data of ocean surface temperature and produces daily averaged SST data over a grid with 1 km resolution using a 2-dimensional variational data assimilation (2DVAR) algorithm [Chao et al., 2009]. The G1SST uses SST data from the Geostationary Operational Environmental Satellite (GOES), Advanced Very-High Resolution Radiometer (AVHRR), Moderate Resolution Imaging Spectroradiometer (MODIS), Spinning Enhanced Visible and Infrared Imager (SEVIRI), Advanced Microwave Scanning Radiometer-EOS (AMSRE), Multi-Functional Transport Satellite 1R (MTSAT-1R) radiometer, and in-situ data from moored buoys and drifters in its analysis. The G1SST data is available for the Caribbean Sea and nearshore areas in gridded format with a sampling time of one day. Detailed specifics on the G1SST dataset are provided in table 2.

4.4 Nearshore In-Situ Measurements

While the open ocean circulation is governed by wind forcing and quasi-geostrophic (QG) instabilities, the nearshore circulation is mostly characterized by wind forcing, boundary-layer effects, surface gravity waves, and the impact of shallow coastal bathymetry on open ocean mesoscale flow [Vic et al., 2015, Pineda et al., 2007]. For a numerical model to realistically simulate these nearshore small-scale processes, the resolution of the model has to be sufficiently fine. Due to a finer resolution of 3 km in the AMSEAS model, the AMSEAS permits a more realistic representation of the complex coastal bathymetry compared to the GOFS and PSY4. Moreover, the fine resolution of the AMSEAS also enables it to partially resolve the O(10 km) submesoscale turbulence. Therefore, it is important to explore whether there is any improvement of model performance due to the fine resolution of the AMSEAS, compared to the coarse resolution of the GOFS and PSY4 in the nearshore regions.

The resolution of the OSCAR and AVISO datasets are too coarse to capture the nearshore variability associated with shallow bathymetry. Moreover, the OSCAR dataset does not take the coastal bathymetry into account in the computation of the current velocities. Therefore, a comparison of the model performance for the nearshore surface current velocity will require in-situ data measured in the nearshore areas of the VI and PR. This available in-situ data includes moored-buoy measurements of surface currents and surface temperature by the Caribbean Coastal Ocean Observing System (CariCOOS), and benthic temperature measurements by HOBO temperature data loggers at various coral reef sites near the coastline as part of the Territorial Coral Reef Monitoring Program (TCRMP) [Smith et al., 2015]. The Caribbean Coastal Ocean Observing System (CariCOOS) maintains a number of moored buoys in coastal regions throughout the US Caribbean [Morell et al., 2015]. The buoys provide hourly data on the surface current velocities measured by Acoustic Doppler Current Profilers (ADCPs) and surface temperature measured by CTDs. In our analysis, we use the data from 4 different buoys; the Ponce buoy (17.86^0 N, -66.52^0 W), San Juan buoy (18.47^0 N, -66.1^0 W), St John buoy (18.25^0 N, -64.76^0 W) and the Vieques buoy (18.26^0 N, -65.46^0 W) (figure 3). The temperature at each of these locations were measured at a depth of 1 m below the water line. The ADCP current data at these locations were measured at multiple bins placed 1 m apart along a vertical profile at each location. The shallowest bin is at 2 m from the surface, whereas the deepest bin is at the benthic depth of the location which is 19 m at Ponce, 32 m at San Juan, 44 m at St John, and 30 m at Vieques. The current data that we used in our analysis is a depth average of all the data collected at the bins for each location up to a depth of 30 m from the surface. We chose a depth of 30 m for the depth averaging because the mixed layer in the US Caribbean region varies from 20 m in summer to 60 m in the winter. The model outputs of the current velocities were obtained as a vertical average within the surface mixed layer.

As part of the Territorial Coral Reef Monitoring Program (TCRMP), a program to monitor the status of coral reefs in the US Virgin Islands, HOBO data loggers were used to measure benthic temperature hourly at coral reef sites across the islands [Smith et al., 2015]. In this study, we compare the seasonal temperature variability of TCRMP sites at Jacks Bay, St. Croix, and two offshore Cays in St. Thomas, Savana (18.34^0 N, -65.08^0 W) and St. James (18.29^0 N, -64.83^0 W; figure 3) with the benthic temperature variability from the model outputs at the same locations. The HOBO loggers were placed at the benthic depths of 27 m at Jacks Bay, 16 m at Savana, and 13 m at St James.

5 Validation Techniques

We evaluate and compare the performance of the models with respect to the remotely estimated open-ocean data and the nearshore in-situ data in the US Caribbean in terms of the simulated SSHA, current velocities and the temperature. Due to sparse availability of data on the interior temperature and velocity fields in the Caribbean Sea, a comparison of the model derived interior fields with observed data is not possible. Therefore, we use the available gridded SSHA and surface current velocity datasets from AVISO and OSCAR respectively, and in-situ temperature data from CariCOOS and TCRMP to evaluate the accuracy of the individual model frameworks for the US Caribbean ocean. Our analysis is based on assessing the model performance in terms of the oceanographic properties in the open ocean and nearshore regions that will be useful for operational oceanography stakeholders in the US Caribbean islands (i.e. scientists, managers, fishermen and captains), and have the requisite observed or in-situ data for comparative analysis. As such, we have identified the open-ocean SSHA, mesoscale eddies, both open-ocean (100 km away from the coastlines, depth $\sim$4 km) and nearshore (less than 1 km from the coastlines, depth $\sim$0.5 km) surface currents, and the surface and benthic ocean temperature for our analysis.

The coastal ocean circulation surrounding the islands is heavily influenced by the interaction of shallow coastal bathymetry with the mesoscale eddy variability in the open ocean. Mesoscale eddies can be identified in the AVISO SSHA as large meanders of O(100 km) diameter with a spatial gradient in the SSHA along their periphery. The resolution of the AMSEAS, GOFS and PSY4 models are adequate to resolve the mesoscale eddies in the Caribbean Sea. Hence, we compare the spatial extent of the O(100 km) mesoscale features in these model outputs with the observed features in the AVISO data using the following methods.

5.1 SSHA Analysis

We compare the spatial and temporal variability of SSHA from the AVISO and the model outputs in 2016 using plan view plots and Hovmöller diagrams respectively. A plan view plot shows the spatial variability of an ocean property at a fixed time, whereas the Hovmöller diagram shows the temporal variability of the property along a fixed transect. Using the plan view plots, we examine the mesoscale variability at 4 randomly chosen dates in March, June, October and December 2016 (figure 6). At each of these dates, we identify the O(100 km) mesoscale features in the AVISO SSHA and find out whether the model outputs show similar features at the same locations.

Using the Hovmöller diagrams, we plot the SSHA from the AVISO data and model outputs along a meridional transect (figure 1) in the Anegada passage over a 1-year period in 2016 (figure 7). The Anegada passage is chosen because the flow through the Anegada passage largely governs the local circulation around PR and the VI [Fratantoni et al., 1997]. A comparison of the temporal variability of SSHA in this region can provide valuable insight on the capability of regional ocean models to resolve the local flow around the islands. Using a Hovmöller diagram, we study the temporal variability in the meridional gradient of the AVISO SSHA in the Anegada passage over a 1-year period in 2016.

The temporal variability of the SSHA in the Anegada passage is further studied using the power spectral density (PSD) computed from the time series of the SSHA, averaged over the zonal range from 16^0 to 20^0 (figure 8). We examine the PSD plot to compare the magnitude of the variance of SSHA at different frequencies corresponding to the large and small temporal scales.

5.1.1 Okubo-Weiss parameter

We assess the mesoscale eddy variability from the modeled and observed SSHA using the Okubo-Weiss parameter, a measure of the strength of the vorticity field relative to the strain field [Isern-Fontanet et al., 2003, Okubo, 1970]. The Okubo-Weiss parameter W is given as

$$W = S_n^2 + S_s^2 - \zeta^2 \tag{1}$$

where $S_n = \partial_x u - \partial_y v$ is the compressive strain, $S_s = \partial_x v + \partial_y u$ is the shear strain, and $\zeta = \partial_x v - \partial_y u$ is the relative vorticity. The variables u and v are the barotropic velocities derived from the SSHA. A mesoscale eddy is defined as a closed region of O(100 km) diameter where $W \leq -0.2\sigma$ where σ is the spatial standard deviation of the W field corresponding to the same sign of ζ [Isern-Fontanet et al., 2003]. Therefore, in order to separately identify the cyclonic and anti-cyclonic mesoscale eddies, we calculate the standard deviation σ separately for the regions corresponding to $\zeta > 0$ and $\zeta < 0$. The strain field is defined as a region where $W > 0.2\sigma$, implying that the strain field dominates the vorticity field by strength.

5.1.2 Taylor Diagram

The relative performance of a model output is best evaluated by the extent of the statistical deviation of each output from the observed data and the correlation of each output with the observed data. Taylor diagrams provide an effective means to visualize the statistical deviations and correlations of the model outputs. A Taylor diagram [Taylor, 2001] is a polar coordinate representation of the following statistical measurements: root mean square deviation ($RMSD$) of the model output from the observed data, cross-correlation (R) of the model output and the observed data, and the standard deviation (σ) of the model output. The $RMSD$ of the model output with respect to the observed data is calculated as

$$RMSD = \left\{ \frac{1}{N} \Sigma_{n-1}^{N} \left[(h_n - \overline{h}) - (o_n - \overline{o}) \right]^2 \right\}^{1/2} \tag{2}$$

where h and o are the model output and the observed dataset respectively and N is the sample size. The overline represents the mean.

The standard deviation of the model output is calculated as

$$\sigma = \sqrt{\frac{1}{N} \Sigma_{n=1}^{N} (h_n - \overline{h})^2} \tag{3}$$

The cross-correlation of model output with the observed data is calculated as

$$R = \frac{1}{\sigma_h \sigma_o} . \frac{1}{N} \Sigma_{n=1}^{N} (h_n - \overline{h})(o_n - \overline{o}) \tag{4}$$

where σ_h and σ_o are the standard deviations of the model output and the observed data respectively. The $RMSD$, σ and R satisfy the following relationship:

$$RMSD^2 = \sigma_h^2 + \sigma_o^2 - 2\sigma_h\sigma_o R \tag{5}$$

In a Taylor diagram (figure 4), each model output and the observed data are represented by specific markers. The observed data marker lies at the base line where the correlation is 1, and the radial distance of each model output marker from the observed data marker denotes the $RMSD$. The distance of each marker from the center of the radial axis denotes the standard deviation σ of the model output or observed data. The arc length along the azimuthal axis (circumference) denotes the cross-correlation coefficient between the model output and the observed data. The performance of the model is interpreted from the relative distance of the model's marker to the marker for the observed data. A larger radial distance from the origin implies a higher standard deviation, indicating that the model output contains more small-scale variability and is noisier than the observed data [Oke et al., 2012]. A shorter distance of the model output marker from the observed data marker implies a lower $RMSD$ and a higher correlation with respect to the observed data. Both higher correlation and lower $RMSD$ can be interpreted as better model performance. Henceforth, the assessment of the model performance is based on how similar the model output is to the observed data, and therefore is confined to the resolution of the available observed data.

We evaluate the model performance in terms of the SSHA, surface current velocities and sea-surface temperature (SST) by comparing the statistical deviations and cross-correlations of the model outputs with respect to the gridded satellite data. For the SSHA data, we conduct two separate analysis using Taylor diagrams for the model outputs in the Caribbean Sea and along a meridional transect in the Anegada passage (figure 1). Prior to the Taylor diagram analysis, the modeled SSHA outputs and the AVISO dataset are prepared in the following manner: (i) at each sampling time, the model output is re-mapped to the horizontal latitude-longitude grid of the AVISO dataset; (ii) for each model output and the AVISO dataset, the 1-dimensional arrays along the time-axis at each of the grid points on the re-mapped domain, are concatenated to form a single 1-dimensional flattened array; (iii) Standard deviation, RMSD and cross-correlation coefficients were calculated using the flattened 1-dimensional arrays of the model outputs and the observed datasets.

5.1.3 Power Spectral Density (PSD)

The contribution of submesoscale and quasi-geostrophic mesoscale turbulence to the variance of the momentum and scalar fields can be estimated using the power spectral density (PSD) of the data as a function of the wavenumber. With enhanced spatial resolution in the satellite observations and numerical models, the variance of different oceanographic properties like the sea-surface temperature (SST), current velocity or the sea-surface height anomaly (SSHA) had been discovered to be mostly governed by O(10 km) submesoscale turbulence along with O(100 km) mesoscale quasi-geostrophic turbulence [Callies and Ferrari, 2013]. In numerical models with a coarse resolution of O(10 km), the velocity variance is mostly dominated by quasi-geostrophic mesoscale turbulence, which results in the PSD being proportional of κ^{-3} where κ is the wavenumber. In contrast, submesoscale turbulence results in the velocity and tracer variances to be proportional to κ^{-2}, which had been noted in fine-resolution glider measurements and numerical ocean models [Callies and Ferrari, 2013, Brannigan et al., 2015, Castro et al., 2017]. On a logarithmic plot of the PSD as a function of the wavenumber, submesoscale turbulence results in a flatter spectral slope compared to mesoscale turbulence.

We compared the spatial variance of the current velocities, SSHA and SST from the model outputs at different spatial scales using the PSD (figure 5). For each data, the PSD is calculated as a function of the longitudinal wavenumber, followed by averaging over the entire range of latitudes and sampling times available in the data.

5.2 Surface Current Velocities

Model performance of the simulated surface current velocities is assessed for both the open ocean and nearshore coastal waters. Open ocean refers to the regions of the Caribbean Sea surrounding the islands where the deep bottom bathymetry has negligible impact on the surface flow. Nearshore refers to the regions near the coastline where the flow is governed by the interaction of shallow coastal bathymetry and the open-ocean mesoscale flow. For the open ocean, we use Taylor diagrams to compare the statistical deviations and correlations of the simulated current velocities with respect to the OSCAR current velocities at the surface. However, due to coarse spatial resolution and lack of consideration of shallow bathymetry in the computation of the current velocities, the OSCAR data is unreliable for the comparative analysis of surface currents in the nearshore areas. Therefore, we compare time-series data of in-situ surface current velocity measured by a subset of the CariCOOS buoys moored near the coastline with the model outputs at the same locations (figure 3). Details on the CariCOOS buoy data is discussed in section 4.4. For both the open ocean and nearshore analysis, we do a comparison of the statistical variability of the surface currents using Taylor diagrams. For the open ocean Taylor diagram, (i) the model outputs are re-mapped to the grid corresponding to the OSCAR data; (ii) the OSCAR data and model outputs are flattened to 1-dimensional arrays by concatenating all the time series of data at each and every grid point in the re-mapped domain. For the nearshore analysis, we construct separate Taylor diagrams for the time series of the surface current data at 4 different buoys at Ponce, San Juan, Vieques and St John respectively.

The temporal variability in the nearshore surface currents is further studied by comparing the magnitude of the variance of the current velocities at different time scales using PSD plots of the velocity variance from the buoy data compared with the model outputs at the same locations. We study the PSD plots from 4 different CariCOOS buoys; Ponce, San Juan, Vieques and St John (figure 13).

5.3 Surface Temperature Variability

Marine biological production in the upper ocean is heavily influenced by the seasonal warming and cooling of the surface boundary layer due to surface heat fluxes [Behrenfeld and Falkowski, 1997]. The summertime warming and wintertime cooling of the boundary layer had been noted in both observations and numerical simulations [Behrenfeld and Falkowski, 1997, Behera et al., 2000]. Since the SST is a good representative of the bulk temperature of the upper ocean boundary layer [Price et al., 1986], a comparison of the seasonal variability of the modeled SST provides an insight on the capability of the models to accurately represent the seasonal warming and cooling of the boundary layer. We conduct two separate comparisons for the open ocean and nearshore SST variability. For the open ocean, we (i) re-map the SST data from the model outputs to the G1SST domain, then (ii) flatten the re-mapped data by concatenating the time arrays at each and every grid points in the re-mapped domain. These flattened arrays are used to prepare a Taylor diagram to compare the standard deviation, $RMSD$ and cross-correlation of the model outputs with respect to the G1SST data in the Caribbean Sea.

We further compare the open-ocean SST variability using a PSD plot of the model outputs and the G1SST data. The PST plot for the SST is prepared as a function of the longitudinal wavenumber, and is averaged over the full range of latitudes and sampling times in the data (figure 5).

For the nearshore analysis, we compare time series data of the temperature measured at the CariCOOS buoys and HOBO loggers located near the coastline with model outputs at the same locations. The CariCOOS buoys measure the surface temperature, whereas the HOBO loggers measure benthic temperature at nearshore coral reef sites. We evaluate the model performance by comparing probability density functions (PDF) of the model error, where the model error is the absolute value of the difference between model output and the buoy data. The x-axis on the PDF plots denotes the maximum value of each bin that corresponds to the range of error with a bin size of 0.1 units (figure

15,16). The y-axis in the PDF plots denotes the number of points lying within each error bin divided by the total number of points in the time series. The relative performance of the model outputs is determined by estimating which model has the highest percentage of points in the bin corresponding to the lowest error.

To compare the seasonal variability of the benthic temperature in the nearshore regions, we select three coral reef sites with the available HOBO logger data at Jacks Bay, Savana and St James (figure 3). We compare the temperature measurements at these sites with the model outputs at the same locations using the PDF calculated from the errors in modeled temperature outputs (figure 16).

6 Results

Our analysis shows that in the open ocean regions of the US Caribbean, the cross-correlation of the SSHA and surface currents between the model outputs and observed data is highest for the PSY4 and lowest for the AMSEAS. The AMSEAS model, despite having a finer resolution, does not adequately simulate the mesoscale flow in the open ocean regions. In the nearshore regions, none of the model outputs show a strong correlation with the in-situ buoy measurements of the surface current velocities. The SST from both the open-ocean and nearshore model outputs strongly correlate with the observed data in terms of the seasonal variability. The results are discussed in detail below.

6.1 SSHA

Model performance of the SSHA variability is compared in the Caribbean Sea and along a meridional transect in the Anegada Passage using two separate Taylor diagrams (figure 4a,4b) over a 1-year long period in 2016. The Taylor diagram of the SSHA in the Caribbean Sea indicates that the highest cross-correlation (0.81), lowest $RMSD$ (0.59) and lowest standard deviation (0.08) between modeled and observed SSHA were found for the PSY4. The AMSEAS and GOFS SSHA form similar correlation coefficients of 0.65 and 0.62 with the AVISO respectively. The standard deviations of the AMSEAS, GOFS and AVISO were 0.12, 0.11 and 0.08 respectively. One of the reasons for a larger standard deviation between 2 models with the same resolution, is the implementation of a weaker eddy viscosity which results in a stronger variance in the outputs [Ramachandran et al., 2013].

The contribution to the variance of SSHA by the processes associated with different spatial scales is studied using a power spectral density (PSD) of the SSHA as a function of the wavenumber (figure 5). A comparison of the PSD of the SSHA at different spatial scales shows that within a range of 10 km to 100 km, the PSD of the AMSEAS SSHA has the highest magnitude, and is followed by the PSD of the GOFS, PSY4 and the AVISO SSHA (figure 5). The AMSEAS SSHA also shows a higher variance at scales larger than 100 km which is due to the combined influence of O(100 km) mesoscale eddies and radially coherent baroclinic tides of wavelength in the range of 100 km to 180 km (figure 5) in the Caribbean Sea [Zaron, 2019]. The GOFS and PSY4 SSHA show a slightly higher variance compared to the AVISO data at scales larger than 100 km, which is synonymous with the higher peaks and deeper troughs of the mesoscale features in the GOFS and PSY4 outputs (figure 5a). The PSD curve for the AMSEAS SSHA shows a slope of κ^{-3} (κ is the wavenumber) at spatial scales near 100 km, but falls rapidly with a steeper slope at the lesser scales near 10 km. The slopes of the GOFS and PSY4 PSD are close to κ^{-4} and the AVISO PSD shows the steepest slope larger than κ^{-4}. The steeper slopes of the wavenumber spectra associated with the SSHA indicates the dominance of mesoscale quasi-geostrophic turbulence and reduced influence of submesoscale turbulence in the GOFS, PSY4 and AVISO SSHA [Callies and Ferrari, 2013]. Since the AMSEAS model can partially resolve submesoscale features, it shows a relatively flatter slope in the SSHA PSD compared to GOFS, PSY4 and the AVISO data.

In the Anegada Passage, standard deviations of the GOFS and PSY4 outputs from the AVISO SSHA were nearly equal at 0.035 (figure 4b). The $RMSD$ and cross-correlation of the GOFS with respect to the AVISO were 0.0375 and 0.6 respectively. The AMSEAS correlated negatively with the AVISO and had the highest standard deviation (0.096) and $RMSD$ (0.11), indicating a weaker performance for simulating SSHA in the Anegada passage. The performance of the PSY4 and GOFS models in the Anegada passage were similar. An analysis of the model performance along a zonal transect in the Anegada passage (plot not shown) showed that the AMSEAS SSHA correlated with the AVISO with a coefficient of 0.3, whereas the PSY4 and GOFS showed cross-correlation coefficients of 0.65 and 0.45 respectively. We infer from this analysis that changing the orientation of the transect in the Anegada passage alters the values of the statistical quantities, but does not affect the relative performance of the model outputs.

The SSHA contours in the plan view plots developed from the AVISO dataset shows prominent mesoscale features (figure 6). These notable mesoscale features in the AVISO data include the O (100 km) cyclonic eddy on 16th March at the southern edge of the contour plot within latitudes 13.5^0 - 15^0 N; the O(100 km) anti-cyclonic eddy near the southern edge within latitudes 13.5^0 - 15^0 N on 13th June and the O(100 km) cyclonic eddy near the southern edge within latitudes 13.5^0 – 15^0 N on 17th October (figure 6). The clear display of these features in the three model outputs indicates the likelihood that the GOFS, PSY4 and AMSEAS resolve most mesoscale features observed in the open-ocean regions of the Caribbean sea observed in the AVISO dataset. Apart from these mesoscale features, the SSHA from the AMSEAS output also shows O(10 km) small-scale meanders which are absent in the GOFS, PSY4 and AVISO. These small-scale features are a consequence of finer grid resolution and weaker eddy viscosity that permits instabilities at scales finer than the mesoscale spatial range [Ramachandran et al., 2013].

Apart from the O(100 km) mesoscale eddies and O(10 km) small-scale undulations in the AMSEAS SSHA, we also observe radially propagating ripples that appear to originate from the south-east vertex of the domain. These ripples are internal baroclinic tides propagating radially outward from the Aves Escarpment (latitude 13^0N longitude 62^0W), which is a mid-ocean ridge in the Caribbean Sea to the west of the lower Antilles islands (figure 1). During the periodic flow of tidal currents over the steep topography of the Aves ridge, vertical oscillation of the isopycnal surfaces of the stratified ocean leads to the formation of baroclinic tides [Jithin et al., 2020]. Ripples formed by baroclinic tides at the Aves ridge have been observed on the sea surface in images captured by the MODIS Terra and Aqua satellites during sun-glint conditions [Alfonso-Sosa, 2013]. Due to the implementation of the OTIS tidal package in the AMSEAS model framework, such baroclinic tidal ripples propagating from the Aves ridge are also simulated by the AMSEAS model in the Caribbean Sea [Zaron, 2019]. Since the GOFS and PSY4 do not implement tidal forcing, we do not observe such baroclinic tidal ripples in their outputs.

A Hovmöller diagram of the AVISO SSHA along the transect shows a consistently positive meridional gradient in the SSHA from May to December 2016 for the GOFS and PSY4 outputs. This same positive trend, however, does not appear in the Hovmöller diagram of the AMSEAS output (figure 7). The model outputs also show small-scale temporal fluctuations in the SSHA that correspond to a stronger variance compared to the AVISO at frequencies higher than $1/10\ \mathrm{day}^{-1}$, as shown in the temporal power spectral density (PSD) plot (figure 8). The PSY4 SSHA variance is weaker in magnitude than the GOFS and AMSEAS at frequencies higher than $1/10\ \mathrm{day}^{-1}$, which is due to the combined influence of stronger eddy viscosity and the coarser resolution of the PSY4 model for the US Caribbean region [Ramachandran et al., 2013]. The variance in the SSHA from the AMSEAS also shows prominent tidal maxima at the diurnal (S1 and K1) and semi-diurnal (M2 and S2) frequencies. The GOFS and PSY4 do not show similar tidal maxima due to the lack of tidal forcing implemented in their simulations.

6.1.1 Analysis using Okubo-Weiss parameter

The mesoscale eddy variability from the model outputs is compared with that from the AVISO data using the Okubo-Weiss parameters derived from the SSHA (figure 9). Since the AMSEAS SSHA are contaminated with internal tidal oscillations (figure 6), we remove the tidal oscillations and the small-scale processes by using a 2-dimensional spatial lowpass filter with a cutoff wavenumber of 1/30 km^{-1}. The GOFS and PSY4 SSHA does not require filtering since they do not implement a tidal model.

Notable mesoscale features in the AVISO contour plots (figure 9) are a cyclonic eddy within latitudes 13.5^0 – 15^0 N surrounded by a strain field on 16th March, an anti-cyclonic eddy near the southern edge within latitudes 13.5^0 – 15^0 N surrounded by a strain field on 13th June, and a cyclonic eddy near the southern edge within latitudes 14^0 – 15^0 N on 17th October and a cyclonic eddy near the northwest vertex on 14th December. These mesoscale structures also appear in the PSY4 and GOFS model outputs of the Okubo-Weiss parameter. The lowpassed AMSEAS outputs also show the large anti-cyclonic eddy at 13th June and the cyclonic eddy at 16th March. However, the mesoscale features appearing during 17th October and 14th December in the lowpassed AMSEAS SSHA, do not match with the AVISO data in terms of their locations. The contrast in the variability of the mesoscale eddies in the AMSEAS and the AVISO outputs, could be attributed to the fact that small-scale features permitted by the AMSEAS model's fine resolution deteriorates the simulated mesoscale variability [Sandery and Sakov, 2017].

6.2 Surface Current Velocities

We conduct two separate comparisons for the model performance in terms of simulating the surface currents in the open ocean and the nearshore regions of the US Caribbean ocean.

6.2.1 Open Ocean Current Velocity

Model performance is evaluated regarding the surface current velocity in the OSCAR data using Taylor diagrams to compare the correlation coefficients, $RMSD$ and standard deviation of the model outputs with respect to the OSCAR data in the open-ocean regions of the Caribbean sea for 2016. Taylor diagrams for the open-ocean outputs (figure 10) shows that the highest cross-correlation (0.74 for both zonal and meridional velocities), and the lowest $RMSD$ (0.1 for zonal and meridional velocities respectively) with the OSCAR velocity data were found for the PSY4 (figure 10). The standard deviation between the PSY4 model outputs and the OSCAR data is the lowest among the three model frameworks (0.2 for the zonal and meridional velocities). The AMSEAS output correlates well with the OSCAR data for the zonal velocity with a coefficient of 0.65 but shows a very weak correlation for the meridional velocity with a coefficient of 0.03 (figure 10b). The cross-correlation coefficient between the GOFS and OSCAR data is 0.7 and 0.6 for the zonal and meridional velocities respectively, which lie between the PSY4 and AMSEAS coefficients in terms of their magnitude.

The zonal velocity in the open-ocean regions of the Caribbean sea mostly represents the westward flow of the Caribbean current forced by the inflow of the Atlantic water through the passages between the Antilles islands. The meridional velocity in the Caribbean Sea observed in the model outputs and OSCAR data is representative of the meridional deviation of the westward Caribbean current due to mesoscale and submesoscale turbulence. In the Hovmöller diagram in figure 11, the Caribbean current is observed as a continuous westward flow in the model outputs, with a short-lived eastward flow that arises by the transit of the mesoscale eddies through the domain between the days 150 to 250. The contrast between the correlation of the AMSEAS zonal and meridional velocities, when compared with the OSCAR data, suggests that the AMSEAS model under-performs in the representation of the meridional currents in the Caribbean Sea.

The PSD of the AMSEAS current velocities (figure 5b) show a typical slope of κ^{-3} which is flatter than the GOFS, PSY4 and OSCAR data. The GOFS and PSY4 outputs show a typical slope of κ^{-4}, whereas the OSCAR velocities show a slope steeper than κ^{-4}. In the presence of submesoscale turbulence, we typically observe a slope of κ^{-2} in the momentum and tracer variances provided the spatial resolution of the measurement is sufficiently high to capture submesoscale turbulence over a spatial scale of 500 m to O(10 km) [Callies and Ferrari, 2013, Brannigan et al., 2015]. The κ^{-3} slope of the AMSEAS current velocities indicate that the AMSEAS only partially resolves the submesoscale turbulence in terms of the current velocities. The 10 km resolution in the GOFS and PSY4 models make it impossible for them to resolve submesoscale turbulence, which explains the steeper slopes in the velocity variance PSD from these models.

6.2.2 Nearshore Current Velocity

Analysis of the Taylor diagrams for the nearshore surface current velocities at the Ponce, San Juan, St. John and Vieques CariCOOS buoys shows that all the model outputs correlate very weakly with the buoy data; cross-correlation coefficients range from -0.2 to 0.45 (figure 12). The AMSEAS current outputs demonstrate larger values of $RMSD$ and larger standard deviation compared to the GOFS and PSY4 outputs which show nearly similar values of the $RMSD$ and standard deviation. A weak correlation coefficient between the modeled current outputs and the OSCAR current data indicates that none of the model outputs exhibit a realistic performance near the coastlines, which is expected given the incapability of the model resolutions to realistically represent the coastal bathymetry.

A temporal power spectral density (PSD) of the eddy kinetic energy (EKE), which displays the variance of the current velocities at the 4 buoy locations, indicates that within a range of $\omega = 10^{-2} - 10^{0}\ \mathrm{day}^{-1}$ (ω is the inverse of the time period), the EKE decays by a factor of approximately ω^{-1} for both the buoy data as well as the model outputs (figure 13), which is similar to the decay shown by HF-radar derived observations of the current velocities on the US west coast [Kim et al., 2011]. At frequencies larger than the inertial frequency, the PSY4 and GOFS outputs demonstrate a steeper rate of decay due to the inability of these models to represent the variance corresponding to small-scale variability spawned by gravity-wave dynamics and 3D turbulence [Ferrari and Wunsch, 2009]. In contrast, the AMSEAS shows a slope of ω^{-1} at frequencies larger than the inertial frequency because the finer resolution of the AMSEAS model framework permits small-scale variability in the velocity fields that are absent in the other two model outputs.

6.3 Temperature Variability

6.3.1 Seasonal SST Variability in the open ocean

The open-ocean SST variability in the US Caribbean is compared with respect to the G1SST data from 2016. The cross-correlation coefficients ranging from 0.89 to 0.91 between each of the model SST outputs and the G1SST data indicates that the seasonal SST variability in the models is strongly correlated with that of the observed data in the Caribbean Sea (figure 14). The $RMSD$ of all the model SST outputs are 0.4 with respect to the G1SST, and the standard deviation is nearly 0.8.

The strong correlation of the simulated SST indicates that all the models perform reasonably well in simulating the seasonal variability of the SST in the Caribbean Sea.

6.3.2 Spectral SST variability

The PSD of SST obtained from the G1SST data varies with a slope of κ^{-2} (figure 5c) near the spatial scale of 100 km, but becomes steeper with a slope of κ^{-3} near the 10 km spatial scale. A tracer spectral slope of κ^{-2} indicates that submesoscale turbulence is the prime contributor to the surface variance of the tracer [Brannigan et al., 2015, Castro et al., 2017]. Due to the fine resolution of

3 km in the AMSEAS model, the AMSEAS SST output showed a typical spectral slope of κ^{-2} (figure 5c) which indicates that submesoscale turbulence strongly dominates the surface variance of the AMSEAS temperature outputs. The GOFS and PSY4 SST outputs show a typical spectral slope of κ^{-3} which is an indicative of the SST variance being dominated by quasi-geostrophic 2D turbulence associated with mesoscale eddies [Callies and Ferrari, 2013].

6.3.3 Nearshore SST Variability

The temperature measurements from the CariCOOS buoys along the northern coastline of PR shows a pattern of annual wintertime cooling from January to March, followed by summertime warming between March and October due to the seasonal variability in the shortwave radiation. A comparison of the temperature time series in 2016 shows that the seasonal variability in the SST seen in the buoy data is clearly replicated by all the model outputs (figure 15).

Figures 15e–h show the PDF of the model error at the 4 different CariCOOS buoy locations (Ponce, San Juan, St John and Vieques). The x-axis denotes the maximum value of each bin corresponding to the range of error with a bin size of 0.1 units. At the St John, Vieques and Ponce buoys, the PSY4 shows the highest percentage of points (54%, 52%, 34%) lying within the bin corresponding to the lowest level of error which is 0.1. At an intermediate error range of 0.5 to 0.9, the PSY4 shows the lowest percentage of points. At the San Juan buoy, the AMSEAS shows better results with the highest percentage of points (30%) within the 0.1 error bin, and the lowest percentage of points at between the 0.7–0.9 error bins.

The temperature time series plots from the HOBO loggers at the coral reef sites show similar summer warming and winter cooling patterns (figure 16a,c,e) as the temperature data recorded at the CariCOOS buoys (figure 15). This similarity between the CariCOOS buoy and HOBO logger datasets is because the shallow depths of the coral reef sites at Jacks Bay, Savanna and St James (14 m, 9 m and 15 m) are within the upper ocean boundary layer where there is a strong response to the seasonal variability of the atmospheric heat fluxes. The simulated temperature from the model outputs at the corresponding coral reef locations also show a similar seasonal variability (figure 16a,c,e). The PDF plot of the model errors shows that at Jacks Bay and St James, the AMSEAS forms a higher fraction of points (0.24 an 0.26 respectively) corresponding to the lowest error bin, whereas at Savana the GOFS forms a higher fraction of points (0.21) at the same bin (figure 16b,d,f).

7 Discussion

This work explores the strengths and weaknesses of the currently operational ocean model frameworks specific to the US Caribbean coastal ocean: the GOFS at $1/12^0$ resolution, the PSY4 at $1/12^0$ resolution and the AMSEAS at $1/36^0$ resolution. The GOFS and AMSEAS use the NCODA, and the PSY4 uses the SEEK filter for assimilating observed data to the outputs. We conduct a series of comparative analysis of the simulated ocean properties from these model frameworks with the corresponding observational data for the Caribbean Sea, which includes the SSHA from AVISO satellite altimetry, surface current velocities from the OSCAR, and interpolated surface temperature estimates by the G1SST from various satellite measurements. While these observational datasets are also available for the coastal ocean surrounding Puerto Rico and the Virgin Islands, the coarse resolution of the data around the islands makes them less reliable for representing the nearshore ocean properties. Therefore, we compared the simulated nearshore temperature and current velocities with in-situ time series data of the temperature and velocities measured at the moored buoys operated by CariCOOS, and time series of temperature measurements using HOBO loggers. All the observed satellite and in-situ data and model outputs used in our analysis are from the year 2016.

In the open ocean regions of the Caribbean Sea, lowest $RMSD$ and highest cross-correlation of the PSY4 outputs with respect to the observed data suggests that the PSY4 produces the most realistic representation of the mesoscale variability in the SSHA. The GOFS model also produces realistic outputs, but with a slightly weaker correlation coefficient and a slightly larger variance than the PSY4 outputs due to the implementation of a weaker eddy viscosity. The temporal variability of the PSY4 SSHA along the transects in the Anegada passage, are also the most realistic compared to the other model outputs. The AMSEAS model produces realistic open-ocean outputs of the SSHA and the zonal current velocities, but fails to produce a realistic SSHA output in the Anegada passage.

In terms of the open-ocean surface current velocities, the PSY4 and GOFS produce the most realistic outputs when compared to the OSCAR data, with the PSY4 showing slightly higher correlation coefficients than the GOFS. The zonal currents in the OSCAR data are majorly dominated by the westward flowing Caribbean current, which is realistically simulated by all the models. However, the AMSEAS model fails to realistically simulate the meridional currents which are formed by the meridional deviation of the Caribbean current due to submesoscale and quasi-geostrophic mesoscale turbulence.

The under-performance of the AMSEAS model in the open-ocean regions of the Caribbean sea, despite it's fine resolution, is attributed to the following reasons:

- The AMSEAS model only partially resolves submesoscale turbulence, and is therefore inadequate to represent the full spectrum of submesoscale turbulence which spans over a range of spatial scales from 500 m to O(10 km).
- The NCODA data assimilation system, used by the AMSEAS, is tuned to constrain the model outputs towards the observed data on the order of spatial scales equivalent to or larger than the mesoscales [Carrier et al., 2019], and is therefore not effective on the submesoscale characteristics of the flow.
- There are no realistic submesoscale variability in the gridded observed data assimilated by the NCODA due to coarse resolution.
- Submesoscale turbulence permitted by the AMSEAS model's fine resolution deteriorates the model output's mesoscale variability due to inverse energy cascade associated with the submesoscales [Sandery and Sakov, 2017].

Since the GOFS, AMSEAS and PSY4 models assimilate observed data, the inferences drawn from the comparative analysis are also an indicative of the performance of the data assimilation algorithms used by the model frameworks. We infer from our analysis that for a numerical grid capable of resolving only the mesoscales and larger scales, both the NCODA and the SEEK filter produce similar outputs. The difference of the variance of outputs between the 2 models with the same resolution, depends on the strength of the eddy viscosity used by the models. Since the NCODA is tuned to constrain the model outputs only at the order of the mesoscales, it is ineffective on the submesoscale turbulence generated by the AMSEAS model at a finer resolution of 3 km. Due to inverse energy cascade, the submesoscale turbulence tends to alter the mesoscale variability in the AMSEAS outputs, thus adversely affecting the performance of the AMSEAS model at O(100 km) mesoscales. However, the strongly dominating Caribbean current in the simulated zonal velocity of the AMSEAS model does not appear to be affected by the interference of the submesoscale turbulence. Therefore, the AMSEAS under-performs in terms of the SSHA and the meridional velocities, but produces a realistic simulation of the Caribbean current associated with the zonal velocities.

The nearshore surface current velocities from all the model outputs correlate very weakly with the in-situ measured velocities from the buoys, which is expected given the coarse resolution of the models. The seasonal variability of the surface temperature and benthic temperature, however, is well represented by all the model outputs in the open ocean and the nearshore regions, as is evident from the strong correlation of the modeled SST with the observed G1SST data. The realistic representation of the seasonal SST variability in both the nearshore and open ocean regions occurs largely as a response of the surface boundary layer to the seasonal variability in the atmospheric heat flux due to shortwave radiation [Price et al., 1986]. Since the impact of the shortwave radiation on the surface boundary layer is well simulated by the GOFS, AMSEAS and PSY4 models using different vertical mixing parameterizations, they are all capable of representing the seasonal SST variability at both the nearshore and the open-ocean regions.

Various oceanic applications require realistic estimates of the ocean properties. A comparative analysis of the model performance is necessary to determine which model output is the most suitable for a specific application that requires oceanographic data. Based on our study, the PSY4 outputs are the more suitable for those applications that require realistic estimates of the open-ocean surface current velocities and the SSHA, whereas any of the PSY4, GOFS and AMSEAS outputs can be used for applications that require data on the seasonal temperature variability. For example, to determine the optimum route for ship navigation in the US Caribbean ocean, the user can refer to the PSY4 outputs for the most realistic estimates of the surface currents and SSHA; to study the impact of seasonal warming on coral bleaching, marine ecologists can refer to any of the GOFS, AMSEAS and PSY4 model outputs for realistic estimates of the benthic temperature; the fisheries industry in the US Caribbean regions can refer to the PSY4 outputs to know the location and trajectories of the mesoscale eddies and determine the potential areas with high chlorophyll concentration.

Applications related to marine ecology mostly require nearshore data of the ocean properties; simulating the larval and sediment transport requires nearshore current velocity data; studying the impact of the seasonal temperature changes on coral reef resilience requires data of the nearshore benthic temperature variability at the coral reef sites. It is clear from our analysis that while the nearshore temperature variability outputs from all the models are reliable, the nearshore current velocity data from any of the models are not realistic enough to be useful. Therefore, the necessity to develop a fine resolution modeling system for the Puerto Rico and the US Virgin Islands coastal ocean circulation motivates further research. A fine resolution model that uses the PSY4 open ocean outputs as boundary conditions, the nearshore buoy measurements for assimilation, and surface forcing from a state of the art atmospheric model, can be useful for the marine ecological applications in the US Caribbean ocean.

Acknowledgement

This work was supported by NSF grant # 1355437: Mare Nostrum Caribbean: Stewardship through Strategic Research and Workforce Development. The authors also thank CariCOOS for access to useful datasets, Dr. Miguel Canals-Silander at the University of Puerto Rico-Mayaguez and Dr. Laurent Chérubin at Florida Atlantic University for their valuable insight.

Table 1: Forecast system model parameters

	GOFS	AMSEAS	PSY4
Model	Hybrid Coordinate Ocean Model (HYCOM)	Navy Coastal Ocean Model (NCOM)	Nucleus for European Modelling of the Ocean (NEMO)
Horizontal grid	Orthogonal curvilinear ($1/12^0$)	Orthogonal curvilinear ($1/36^0$)	Tripolar ORCA ($1/12^0$)
Vertical grid	32 levels, (isopycnal in open ocean, terrain following in coastal ocean, z-level in mixed-layer)	40 levels, terrain-following σ coordinates near surface and z-level coordinates below	50 levels, decreasing resolution from 1 m at the surface to 450 m at bottom, 22 levels within upper 100 m.
Advection	multi-dimensional positive advection transport [Smolarkiewicz and Grabowski, 1990]	quasi-third order upwind advection for momentum and scalars [Holland et al., 1998]	energy/enstrophy conserving scheme (momentum) [Arakawa and Lamb, 1981], TVD 2nd order scheme (tracer) [Lévy et al., 2001]
Mixing	2nd order Flux Corrected Transport (FCT) [Zalesak, 1979] (horizontal eddy viscosity 50 $\mathrm{m^2 s^{-1}}$), KPP for vertical mixing	Mellor-Yamada 2.5 vertical mixing, Smagorinsky scheme [Smagorinsky, 1963] for horizontal viscosities	Laplacian isopycnal (tracer) (80 $\mathrm{m^2 s^{-1}}$), biharmonic (momentum) (-1×10^{11} $\mathrm{m^4 s^{-1}}$), turbulence closure 1.5 [Blanke and Delecluse, 1993]
Surface forcing	NAVGEM	15 km Navy COAMPS model	ECMWF
Data assimilation	NCODA with 3DVAR	NCODA with 3DVAR	SAM (reduced-order Kalman filter) with 3DVAR
Data assmilated	SSH anomaly (AVISO), SST (GHRSST), in-situ observations from ships, buoys, XBT, CTD, Argo floats,	same as GOFS	CMEMS (OSTIA SST, sea-ice concentration and SSH), WOA 2013 climatology below 2000 m
Sampling time	3-hourly instantaneous	3-hourly instantaneous	1-hourly instantaneous

Table 2: Gridded ocean datasets

	AVISO	OSCAR	GHRSST
Ocean property	Sea-surface height anomaly (m) (SSHA)	Surface current velocities (m/s)	Sea-surface temperature (SST) (^0C)
Horizontal Grid	$1/4^0$ of latitude	$1/3^0$ of latitude	1 km
source of data	Altimetry measurements from altimeters aboard the TOPEX/Poseidon, Envisat, Jason-1 and OSTM/Jason-2	Interpolation and analysis of SSHA, surface wind velocity and SST data obtained fromsatellite and in-situ measurements	AVHRR, AATSR, SEVIRI, AMSRE, TMI, MODIS, GOES, MTSAT-1R
Temporal averaging	daily averaged	averaged over 5 days	daily averaged

References

Edwin Alfonso-Sosa. First modis images catalog of aves ridge solitons in the caribbean sea (2008-2013). *Ocean Physics Education*, 8, 2013.

A. Arakawa and V. R. Lamb. A potential enstrophy and energy conserving scheme for the shallow water equations. *Monthly Weather Review*, 109(1):18–36, 1981.

AVISO-Altimetry. Aviso user handbook for merged topex/poseidon products, 1996.

D. M. Barker, W. Huang, Y-R. Guo, A. J. Bourgeois, and Q. N. Xiao. A three-dimensional variational data assimilation system for mm5: Implementation and initial results. *Monthly Weather Review*, 132(4):897–914, 2004.

C. N. Barron, A. B. Kara, P. J. Martin, R. C. Rhodes, and L. F. Smedstad. Formulation, implementation and examination of vertical coordinate choices in the global navy coastal ocean model (ncom). *Ocean Modelling*, 11(3-4):347–375, 2006.

S. K. Behera, P. S. Salvekar, and T. Yamagata. Simulation of interannual sst variability in the tropical indian ocean. *Journal of Climate*, 13(19):3487–3499, 2000.

M. J. Behrenfeld and P. G. Falkowski. Photosynthetic rates derived from satellite-based chlorophyll concentration. *Limnology and oceanography*, 42(1):1–20, 1997.

F. Blanc, M. Borra, P. Boudou, S. d'Alessio, P. Gaspar, N. Greenwood, Marseille M. Le Provost Ch, R. Rapp, C. Schgounn, C. K. Shum, et al. Aviso/altimetry,"aviso user handbook for merged topex/poseidon products". Technical report, AVI-NT-02-101,, 1996.

B. Blanke and P. Delecluse. Variability of the tropical atlantic ocean simulated by a general circulation model with two different mixed-layer physics. *Journal of Physical Oceanography*, 23(7):1363–1388, 1993.

F. Bonjean and G. S. E. Lagerloef. Diagnostic model and analysis of the surface currents in the tropical pacific ocean. *Journal of Physical Oceanography*, 32(10):2938–2954, 2002.

Liam Brannigan, David P Marshall, Alberto Naveira-Garabato, and AJ George Nurser. The seasonal cycle of submesoscale flows. *Ocean Modelling*, 92:69–84, 2015.

P. Brasseur and J. Verron. The seek filter method for data assimilation in oceanography: a synthesis. *Ocean Dynamics*, 56(5-6):650–661, 2006.

Jörn Callies and Raffaele Ferrari. Interpreting energy and tracer spectra of upper-ocean turbulence in the submesoscale range (1–200 km). *Journal of Physical Oceanography*, 43(11):2456–2474, 2013.

Matthew J Carrier, John J Osborne, Hans E Ngodock, Scott R Smith, Innocent Souopgui, and Joseph M D'Addezio. A multiscale approach to high-resolution ocean profile observations within a 4dvar analysis system. *Monthly Weather Review*, 147(2):627–643, 2019.

S. L. Castro, W. J. Emery, G. A. Wick, and W. Tandy. Submesoscale sea surface temperature variability from uav and satellite measurements. *Remote Sensing*, 9(11):1089, 2017.

Y. Chao, Z. Li, J. D. Farrara, and P. Hung. Blending sea surface temperatures from multiple satellites and in situ observations for coastal oceans. *Journal of Atmospheric and Oceanic Technology*, 26 (7):1415–1426, 2009.

E. P. Chassignet, H. E. Hurlburt, O. M. Smedstad, G. R. Halliwell, P. J. Hogan, A. J. Wallcraft, R. Baraille, and R. Bleck. The hycom (hybrid coordinate ocean model) data assimilative system. *Journal of Marine Systems*, 65(1):60–83, 2007.

E. P. Chassignet, H. E. Hurlburt, E. J. Metzger, O. M. Smedstad, J. A. Cummings, G. R. Halliwell, R. Bleck, R. Baraille, A. J. Wallcraft, C. Lozano, et al. Us godae: global ocean prediction with the hybrid coordinate ocean model (hycom). *Oceanography*, 22(2):64–75, 2009.

L. M. Chérubin and L. Garavelli. Eastern caribbean circulation and island mass effect on st. croix, us virgin islands: a mechanism for relatively consistent recruitment patterns. *PloS ONE*, 11(3): e0150409, 2016.

L. M. Chérubin and P. L. Richardson. Caribbean current variability and the influence of the amazon and orinoco freshwater plumes. *Deep Sea Research Part I: Oceanographic Research Papers*, 54 (9):1451–1473, 2007.

J. A. Cummings and O. M. Smedstad. Variational data assimilation for the global ocean. In *Data Assimilation for Atmospheric, Oceanic and Hydrologic Applications (Vol. II)*, pages 303–343. Springer, 2013.

Gary D Egbert and Svetlana Y Erofeeva. Efficient inverse modeling of barotropic ocean tides. *Journal of Atmospheric and Oceanic technology*, 19(2):183–204, 2002.

R. Ferrari and C. Wunsch. Ocean circulation kinetic energy: Reservoirs, sources, and sinks. *Annual Review of Fluid Mechanics*, 41, 2009.

D. M. Fratantoni, R. J. Zantopp, W. E. Johns, and J. L. Miller. Updated bathymetry of the anegada-jungfern passage complex and implications for atlantic inflow to the abyssal caribbean sea. *Journal of Marine Research*, 55(5):847–860, 1997.

L. Guerrero, J. Sheinbaum, and J. Candela. Tracking eddies in the caribbean sea using the aviso altimetry analysis. In *Western Pacific Geophysics Meeting, Honolulu, Hawai'i*, pages 16–20, 2004.

J. T. Gunn and D. R. Watts. On the currents and water masses north of the antilles/bahamas arc [netherlands antilles]. *Journal of Marine Research*, 40:1–18, 1982.

R. W. Helber, T. L. Townsend, C. N. Barron, J. M. Dastugue, and M. R. Carnes. Validation test report for the improved synthetic ocean profile (isop) system, part i: Synthetic profile methods and algorithm. Technical Report NRL/MR/7320–13-9364, Naval Research Lab, 2013.

F. Hernandez, L. Bertino, G. Brassington, E. Chassignet, J. Cummings, F. Davidson, M. Drevillon, G. Garric, M. Kamachi, J-M. Lellouche, et al. Validation and intercomparison studies within godae. *Oceanography*, 22(3):128–143, 2009.

R. M. Hodur. The naval research laboratory's coupled ocean/atmosphere mesoscale prediction system (coamps). *Monthly weather review*, 125(7):1414–1430, 1997.

William R Holland, Julianna C Chow, and Frank O Bryan. Application of a third-order upwind scheme in the ncar ocean model. *Journal of Climate*, 11(6):1487–1493, 1998.

Ibrahim Hoteit, Xiaodong Luo, Marc Bocquet, Armin Kohl, and Boujemaa Ait-El-Fquih. Data assimilation in oceanography: current status and new directions. *New Frontiers in Operational Oceanography*, pages 465–512, 2018.

J. Isern-Fontanet, E. García-Ladona, and J. Font. Identification of marine eddies from altimetric maps. *Journal of Atmospheric and Oceanic Technology*, 20(5):772–778, 2003.

AK Jithin, MP Subeesh, PA Francis, and SSV S Ramakrishna. Intensification of tidally generated internal waves in the north-central bay of bengal. *Scientific reports*, 10(1):1–11, 2020.

W. E. Johns, T. L. Townsend, D. M. Fratantoni, and W. D. Wilson. On the atlantic inflow to the caribbean sea. *Deep Sea Research Part I: Oceanographic Research Papers*, 49(2):211–243, 2002.

E. S. Johnson, F. Bonjean, G. S. E. Lagerloef, J. T. Gunn, and G. T. Mitchum. Validation and error analysis of oscar sea surface currents. *Journal of Atmospheric and Oceanic Technology*, 24(4): 688–701, 2007.

S. Y. Kim, E. J. Terrill, B. D. Cornuelle, B. Jones, L. Washburn, M. A. Moline, J. D. Paduan, N. Garfield, J. L. Largier, G. Crawford, et al. Mapping the us west coast surface circulation: A multiyear analysis of high-frequency radar observations. *Journal of Geophysical Research: Oceans*, 116(C3), 2011.

M. Lévy, A. Estublier, and G. Madec. Choice of an advection scheme for biogeochemical models. *Geophysical Research Letters*, 28(19):3725–3728, 2001.

G. Madec. The nemo team (2008) nemo ocean engine. *Note du Pôle de modélisation. Institut Pierre-Simon Laplace (IPSL), France*, 2008.

G. Madec and M. Imbard. A global ocean mesh to overcome the north pole singularity. *Climate Dynamics*, 12(6):381–388, 1996.

P. Marchesiello, J. C. McWilliams, and A. Shchepetkin. Open boundary conditions for long-term integration of regional oceanic models. *Ocean modelling*, 3:1–20, 2001.

J. M. Morell, M. F. Canals, J. E. Capella, L. D. Aponte, J. E. Corredor, R. Watlington, and C. Garcia. Ioos-caricoos: past, present and future of a tropical coastal ocean observing system. In *OCEANS 2015-Genova*, pages 1–4. IEEE, 2015.

P. R. Oke, G. B. Brassington, D. A. Griffin, and A. Schiller. The bluelink ocean data assimilation system (bodas). *Ocean Modelling*, 21:46–70, 2008.

P. R. Oke, G. B. Brassington, J. Cummings, M. Martin, and F. Hernandez. Godae inter-comparisons in the tasman and coral seas. *Journal of Operational Oceanography*, 5(2):11–24, 2012.

A. Okubo. Horizontal dispersion of floatable particles in the vicinity of velocity singularities such as convergences. In *Deep sea research and oceanographic abstracts*, volume 17, pages 445–454. Elsevier, 1970.

J. Pineda, J. A. Hare, and S. U. Sponaugle. Larval transport and dispersal in the coastal ocean and consequences for population connectivity. *Oceanography*, 20(3):22–39, 2007.

J. F. Price, R. A. Weller, and R. Pinkel. Diurnal cycling: Observations and models of the upper ocean response to diurnal heating, cooling, and wind mixing. *Journal of Geophysical Research: Oceans*, 91:8411–8427, 1986.

S. Ramachandran, A. Tandon, and A. Mahadevan. Effect of subgrid-scale mixing on the evolution of forced submesoscale instabilities. *Ocean Modelling*, 66:45–63, 2013.

C. Rowley and A. Mask. Regional and coastal prediction with the relocatable ocean nowcast/forecast system. *Oceanography*, 27(3):44–55, 2014.

P. A. Sandery and P. Sakov. Ocean forecasting of mesoscale features can deteriorate by increasing model resolution towards the submesoscale. *Nature communications*, 8(1):1–8, 2017.

R. Sikhakolli, R. Sharma, S. Basu, B. S. Gohil, A. Sarkar, and KVSR. Prasad. Evaluation of oscar ocean surface current product in the tropical indian ocean using in situ data. *Journal of earth system science*, 122(1):187–199, 2013.

J. Smagorinsky. General circulation experiments with the primitive equations: I. the basic experiment. *Monthly weather review*, 91(3):99–164, 1963.

T. B. Smith, R. S. Ennis, E. Kadison, D. W. Weinstein, J. Jossart, J. Gyory, et al. The united states virgin islands territorial coral reef monitoring program 2015 annual report. *US Virgin Islands: University of the Virgin Islands*, 2015.

P. K. Smolarkiewicz and W. W. Grabowski. The multidimensional positive definite advection transport algorithm: Nonoscillatory option. *Journal of Computational Physics*, 86(2):355–375, 1990.

D. Storkey, E. W. Blockley, R. Furner, C. Guiavarc'h, D. Lea, M. J. Martin, R. M. Barciela, A. Hines, P. Hyder, and J. R. Siddorn. Forecasting the ocean state using nemo: The new foam system. *Journal of operational oceanography*, 3(1):3–15, 2010.

K. E. Taylor. Summarizing multiple aspects of model performance in a single diagram. *Journal of Geophysical Research: Atmospheres*, 106:7183–7192, 2001.

C. Vic, G. Roullet, X. Capet, X. Carton, M. J. Molemaker, and J. Gula. Eddy-topography interactions and the fate of the persian gulf outflow. *Journal of Geophysical Research: Oceans*, 120(10):6700–6717, 2015.

T. Whitcomb. Navy global forecast system, navgem: Distribution and user support. In *2nd Scientific Workshop on ONR DRI: Unified Parameterization for Extended Range Prediction*, 2012.

S. T. Zalesak. Fully multidimensional flux-corrected transport algorithms for fluids. *Journal of computational physics*, 31(3):335–362, 1979.

E. D. Zaron. Predictability of non-phase-locked baroclinic tides in the caribbean sea. *Ocean Science*, 15(5), 2019.

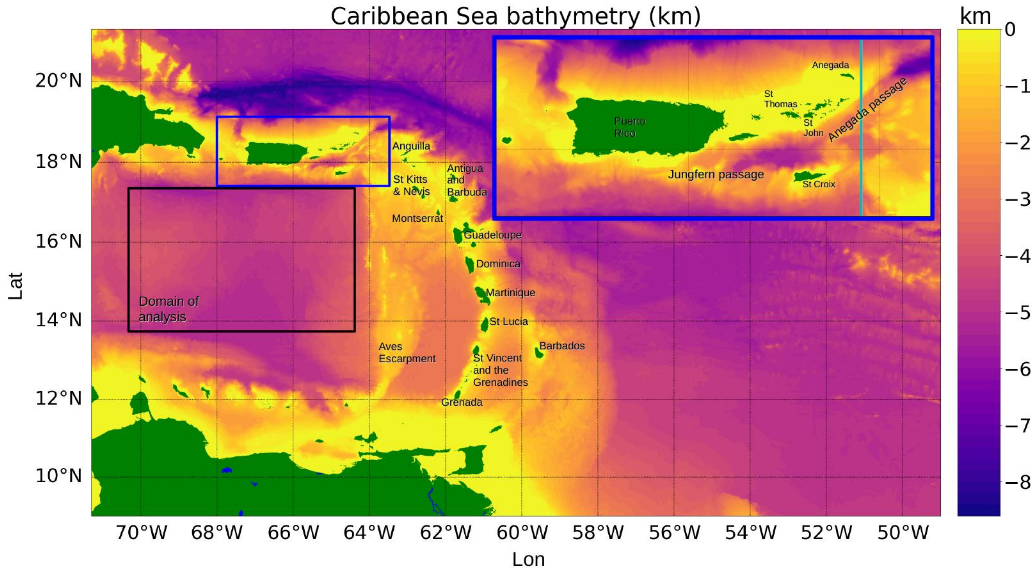

Figure 1: Bathymetry of the northern Caribbean Sea from ETOPO 1 km. Landmasses are denoted by green color. The black rectangle denotes the region where we do the comparative analysis between model outputs. The blue rectangle denotes the domain containing Puerto Rico and the Virgin Islands, and is enlarged to show the islands and Anegada passage in detail.

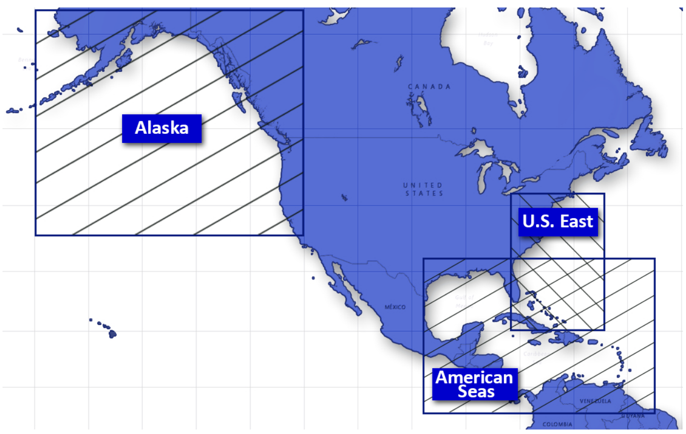

Figure 2: Map showing the regional grids for Alaskan Sea, US East Coast, and Gulf and Mexico and Caribbean Sea covered by the NCOM model. This map is obtained from the NOAA NCOM server.

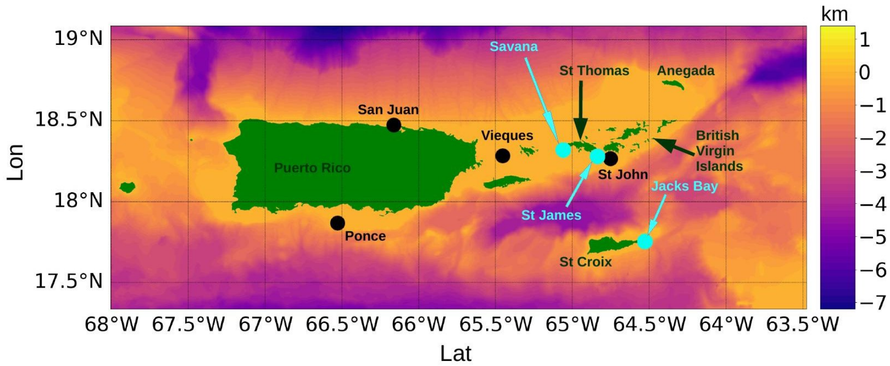

Figure 3: ETOPO 1 km bathymetry of the Puerto Rico and Virgin Islands coastal ocean, with filled circles showing the locations of the CariCOOS buoys (black) at Ponce, San Juan, Vieques, St John, and the TCRMP coral reef sites (indigo) at Jacks Bay, Savanna and St James. The CariCOOS buoys provide in-situ surface currents, and the HOBO loggers at the TCRMP sites provide benthic temperature data.

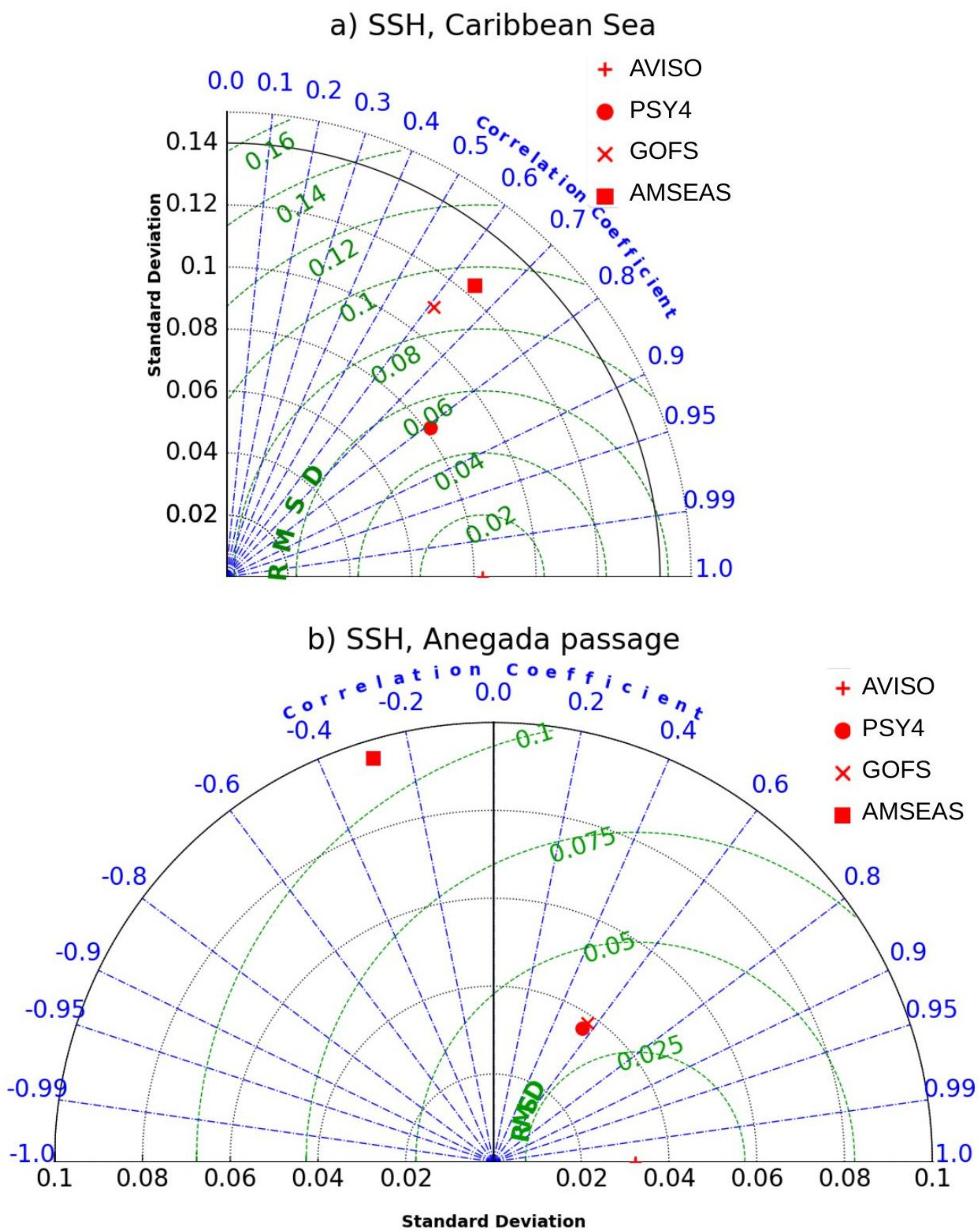

Figure 4: Taylor diagram of the SSHA from the AVISO and the PSY4, GOFS and AMSEAS model outputs in 2016 for Caribbean Sea (plot a), and along a meridional transect in the Anegada passage (plot b). The length along the radial axis denotes the standard deviation. The arc length along the circumference denotes the cross-correlation coefficient of each model output with the AVISO dataset. The model outputs and the AVISO dataset are represented by different markers on each plot. The AVISO marker lies on the x axis, and the length of each model's marker to the AVISO marker denotes the $RMSD$.

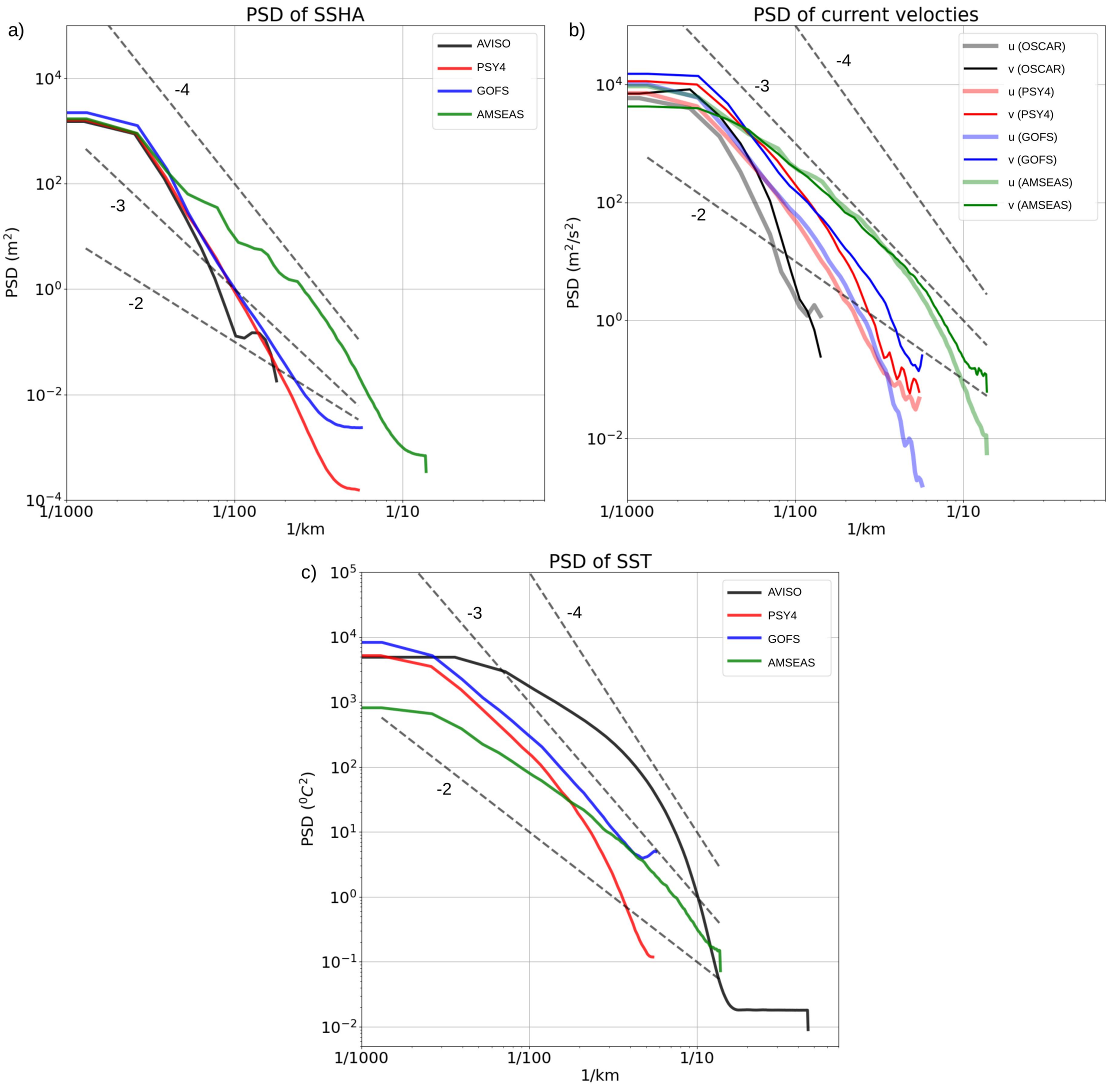

Figure 5: Spatial power spectral density (PSD) of the SSHA (plot a), surface current velocities (plot b) and SST (plot c) of the model outputs compared to the AVISO SSHA, OSCAR current velocities and G1SST temperature respectively. The dashed lines denote the slopes of κ^{-4}, κ^{-3} and κ^{-2} on the loglog plot (κ is the wavenumber).

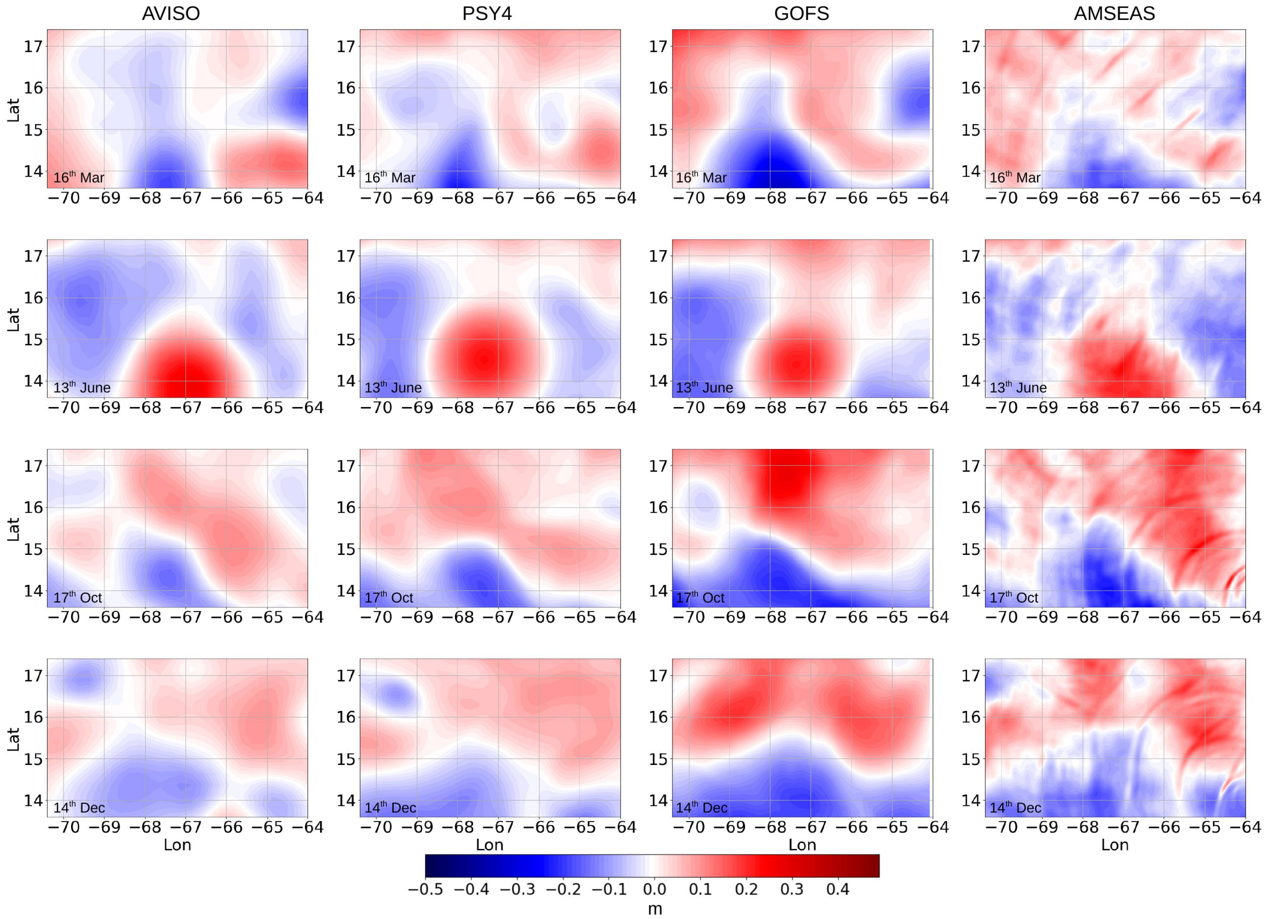

Figure 6: Contour plots showing the sea-surface height anomaly (SSHA) from the AVISO altimetry data and the PSY4, GOFS and AMSEAS models in the Caribbean Sea at 4 randomly chosen dates in 2016. The columns from left to right show the SSHA from the AVISO, PSY4, GOFS and AMSEAS respectively. The rows from top to bottom show the SSHA from the dates 16th March, 13th June, 17th October and 14th December respectively.

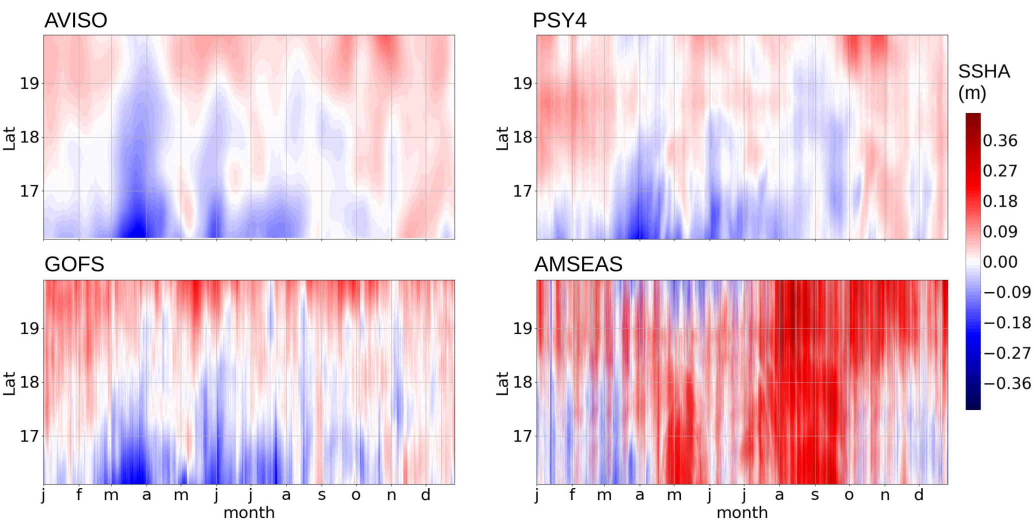

Figure 7: Hovmöller diagram showing the temporal variability of the SSHA from the (a) AVISO, (b) PSY4, (c) GOFS and (d) AMSEAS in 2016 along a meridional transect in the Anegada passage on the east of St John island at longitude 64.2^0 W. The meridional transect is denoted in figure 1 by the indigo line.

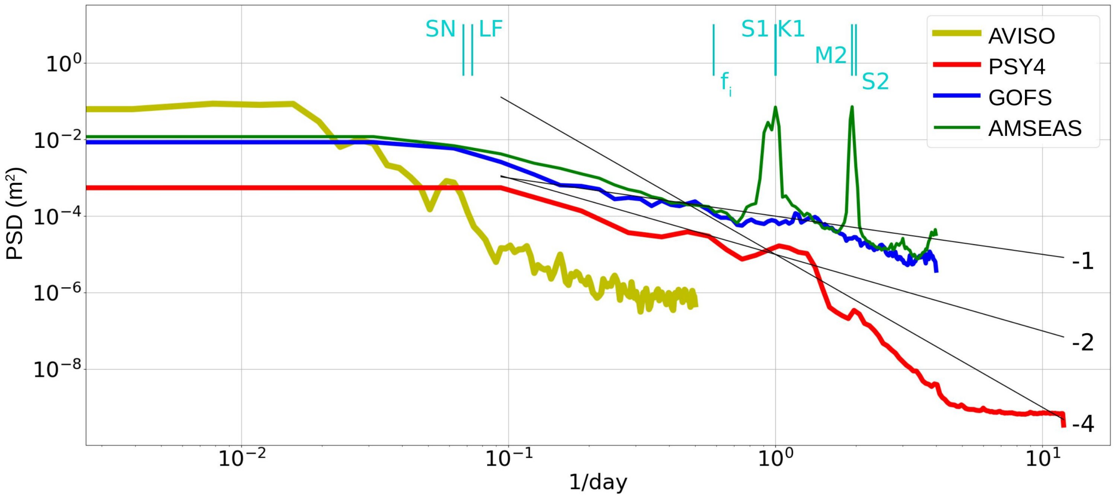

Figure 8: Average power spectral density (PSD) of the time series of the SSHA along a meridional transect in the Anegada passage at latitude 18^0 N. The averaging is done over the range of longitudes from 16^0 to 20^0 N. The tidal frequencies for diurnal (S1, K1) and semi-diurnal (M2, S2) tides are marked in cyan. The variable f_i denotes the inertial frequency corresponding to 40 hours.

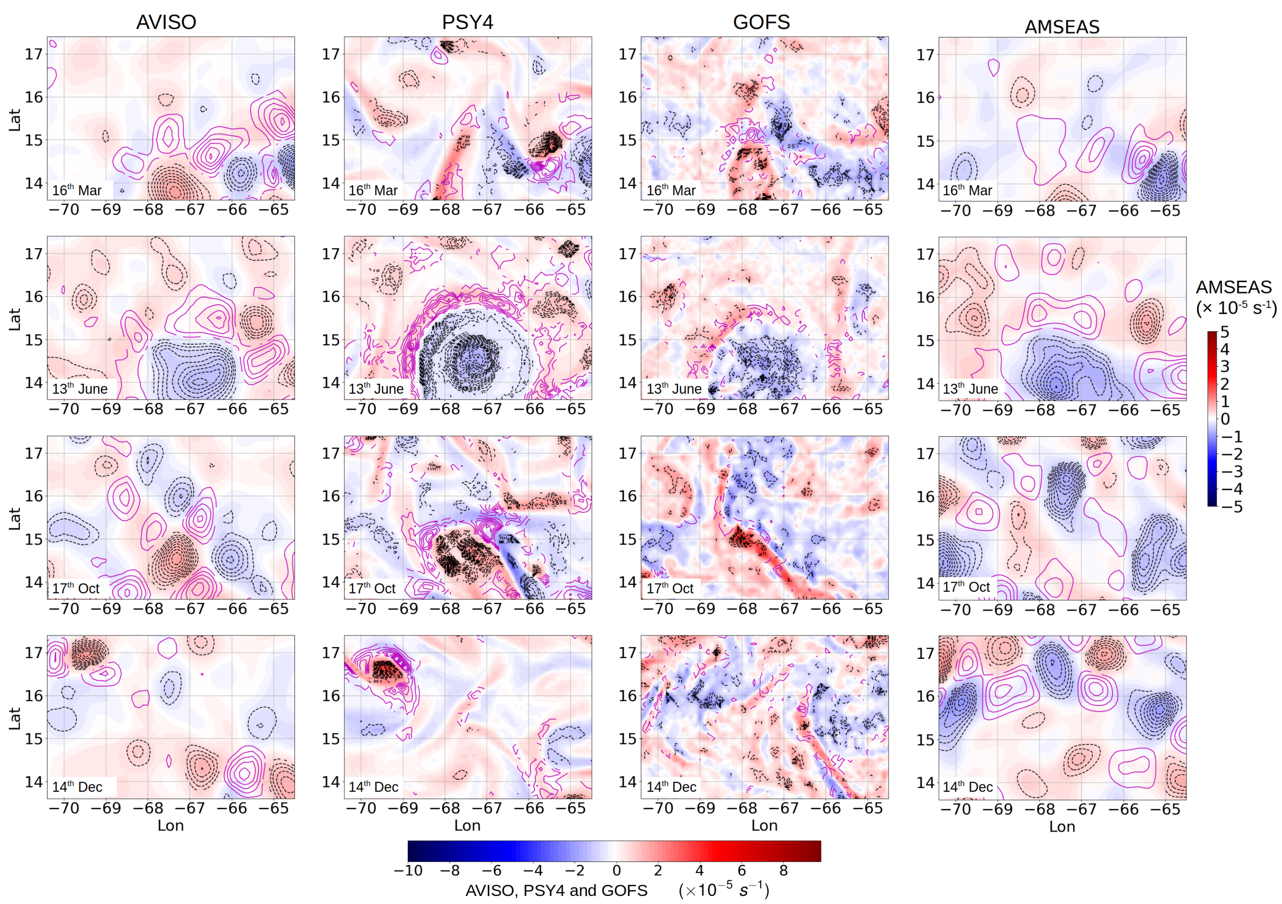

Figure 9: Plan view plots showing the relative vorticity (ζ s^{-1}) in red and blue color and the Okubo-Weiss parameter in black and magenta contour lines. The dashed black lines show the regions where $W < -0.2\sigma$ where σ is the standard deviation of W corresponding to the same sign of the relative vorticity ζ. The solid magenta lines show the regions where $W > 0.2\sigma_W$. From top to bottom, the rows show the contours on 16th March, 13th June, 17th October and 14th December 2016 respectively. The lowpassed AMSEAS contours are shown with a different color scale to highlight the oceanographic features prominently.

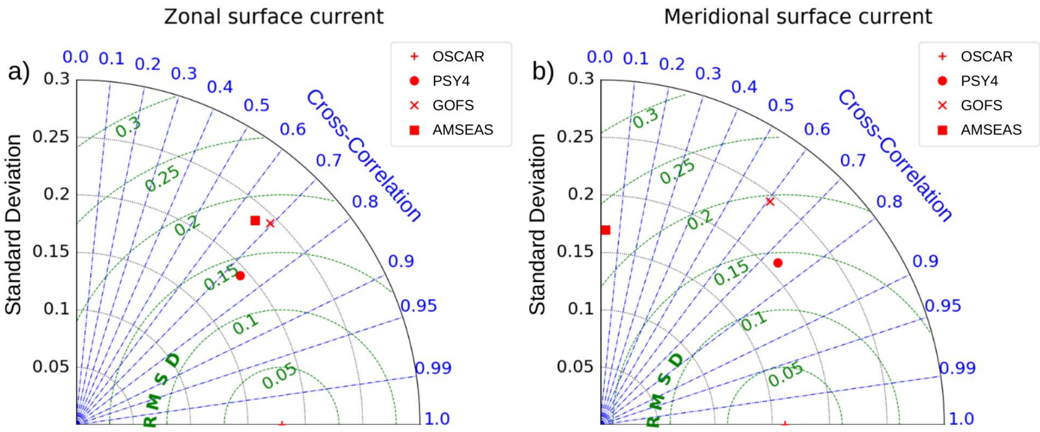

Figure 10: Taylor diagrams of the simulated surface currents from the PSY4, GOFS and AMSEAS with respect to the OSCAR dataset in 2016. Plot a is calculated from the zonal surface currents and plot b from the meridional surface currents. Current velocity from each model output and the OSCAR data are represented by different markers. The radial axis denotes the standard deviation and the azimuthal axis the cross-correlation coefficient. The length of each marker from the OSCAR marker denotes the RMSD.

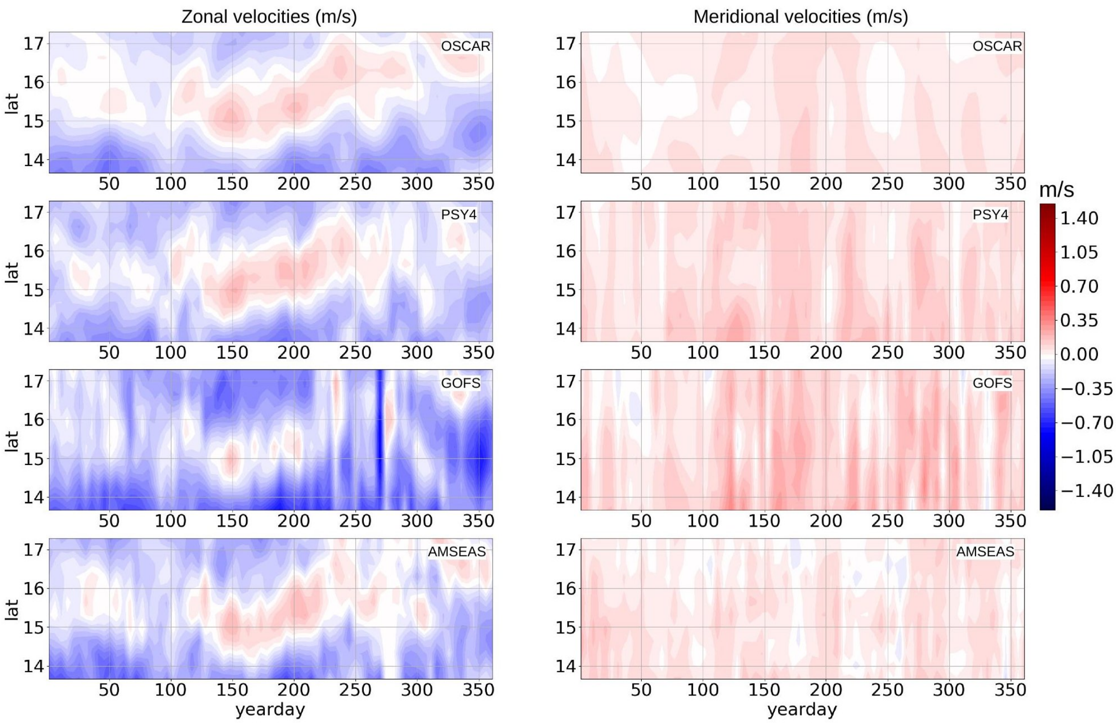

Figure 11: Hovmöller diagrams showing the zonal and meridional velocities from the model outputs and the OSCAR data over a span of 1 year in 2016, averaged over the longitudes. The left and right panels show the zonal and meridional velocities respectively.

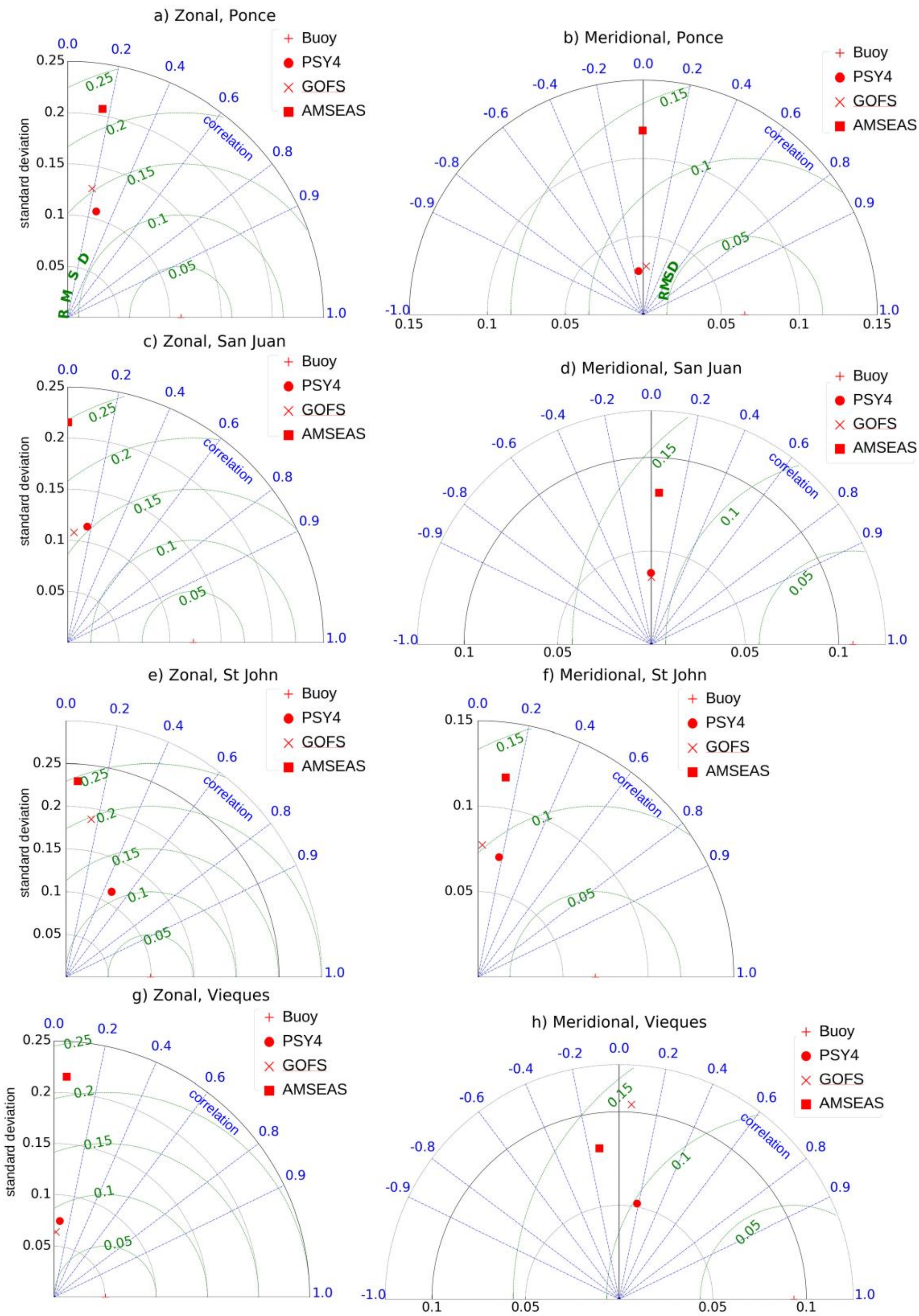

Figure 12: Taylor diagram for the nearshore velocity time series from the in-situ buoy measurements and the PSY4, GOFS and AMSEAS outputs. The left column shows Taylor diagrams for the zonal current velocities, and the right column the meridional current velocities. The rows from top to bottom show the plots for Ponce, San Juan, St John and Vieques respectively.

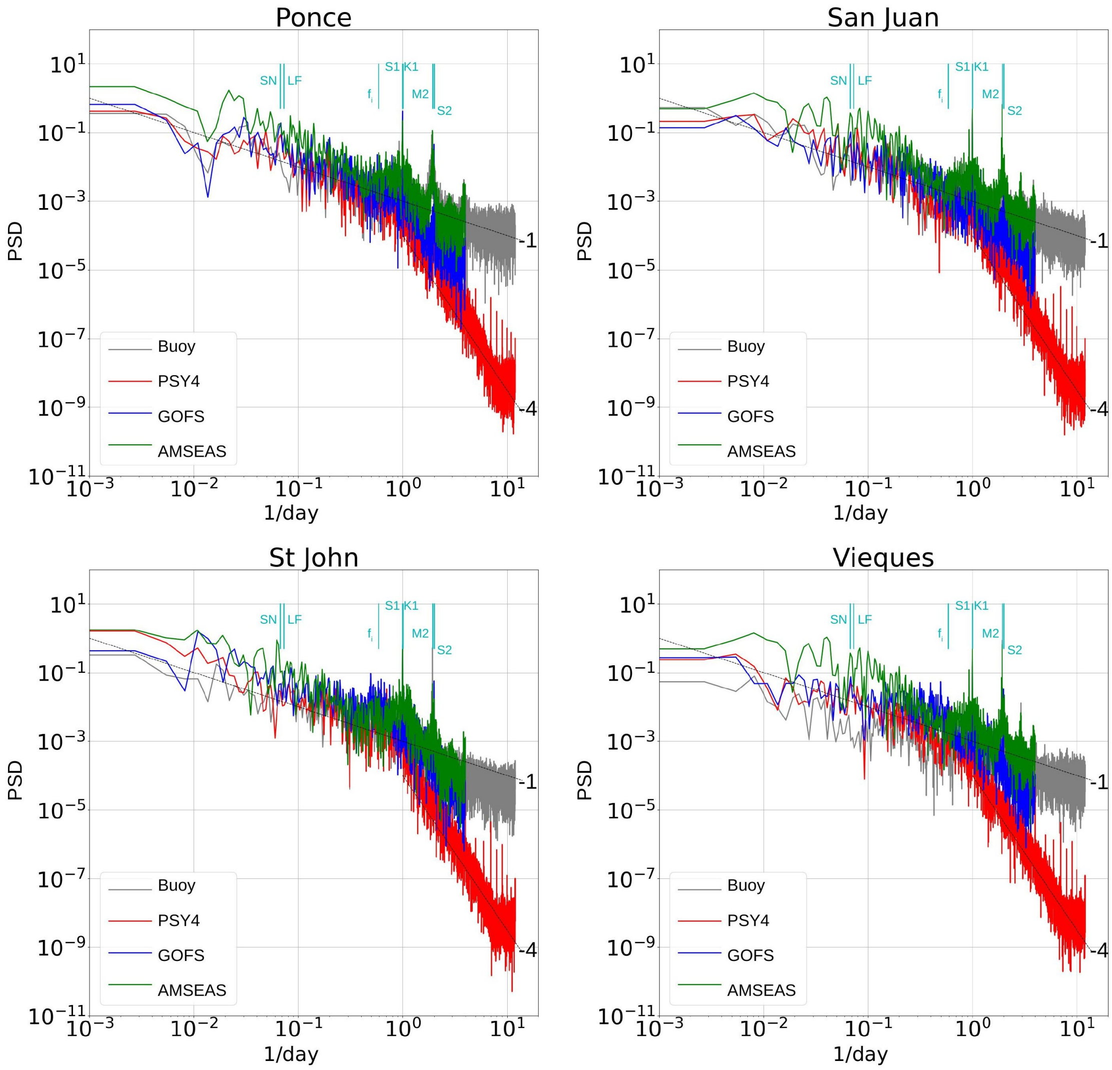

Figure 13: Temporal power spectral density (PSD) of the variance of the surface current velocity measured at the CariCOOS buoys at Ponce, San Juan, St John and Vieques along with model outputs at the same locations for a 1-year long data in 2016. The tidal frequencies for SN (spring-neap), LF (lunar fortnightly), S1, K1, M2 and S2 are marked in cyan. The dashed black lines indicate the slope of the PSD plots.

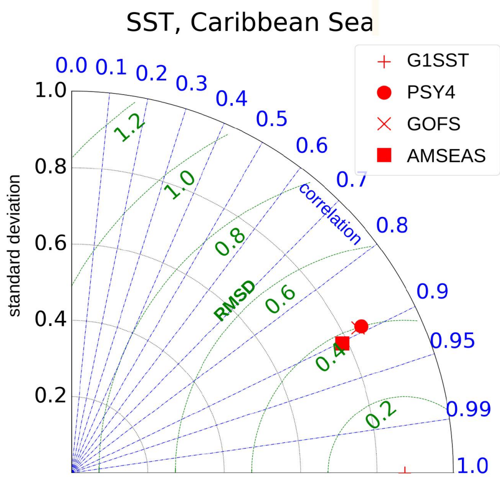

Figure 14: Taylor diagram showing the cross-correlation, standard deviation and $RMSD$ of the SST from PSY4, GOFS and AMSEAS model outputs with respect to the G1SST data in 2016. The geographic range chosen for this analysis is denoted by the black rectangle in figure 3.

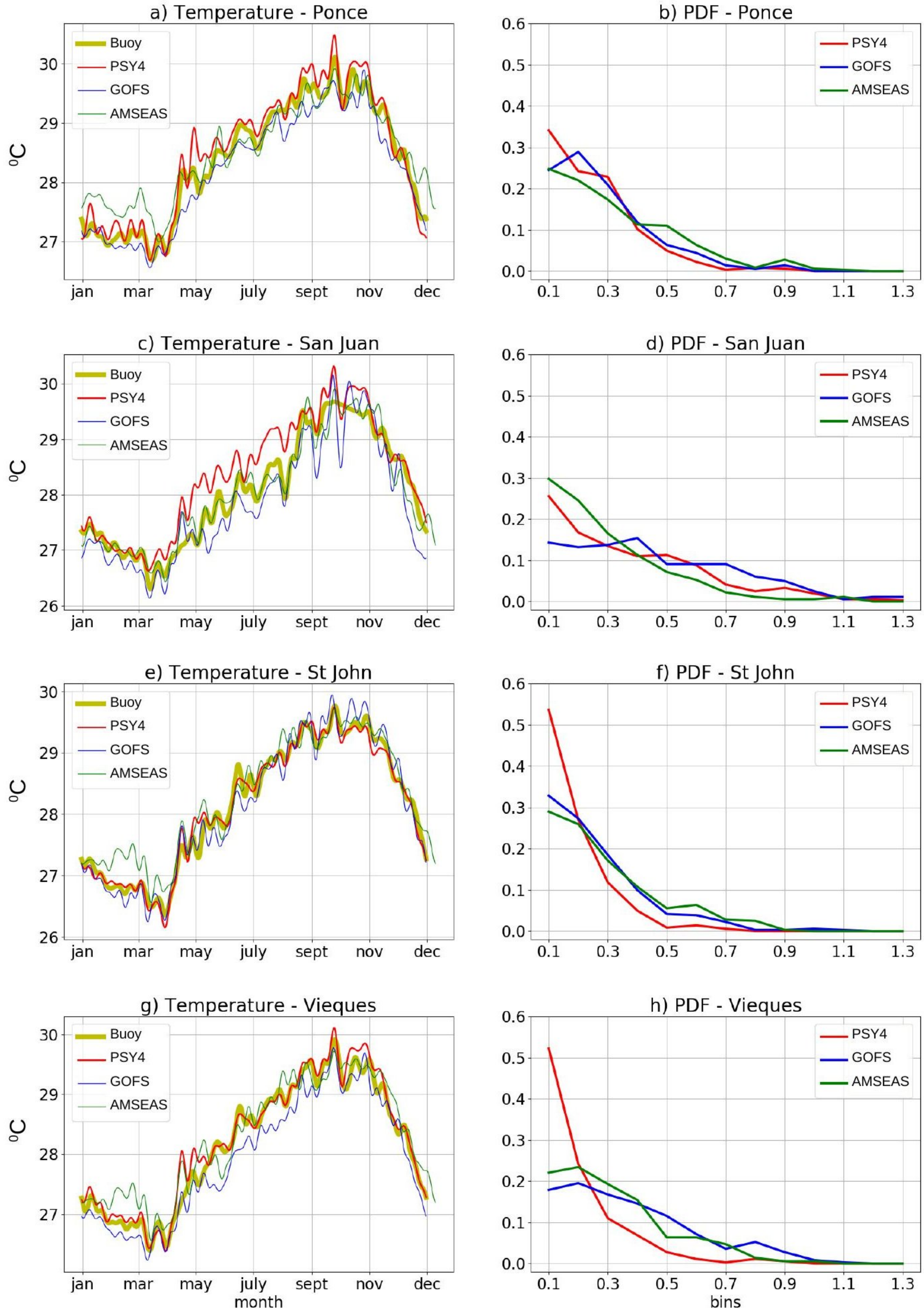

Figure 15: Seasonal variability of the sea surface temperature ^{0}C measured at the CariCOOS buoys at Ponce, San Juan, St John and Vieques, with model outputs at the same locations. The left column shows the time-series of the temperature, low-passed with a cutoff filter of 1 day. The right column shows the corresponding probability density functions (PDF) computed from the model errors. The x-axis in the PDF plot denotes the maximum error value of each bin, with a bin size of 0.1 units. The y-axis denotes the fraction of the number of points lying in a bin, divided by the total number of points in the time series. Refer to section 5.3 for details on the PDF calculation.

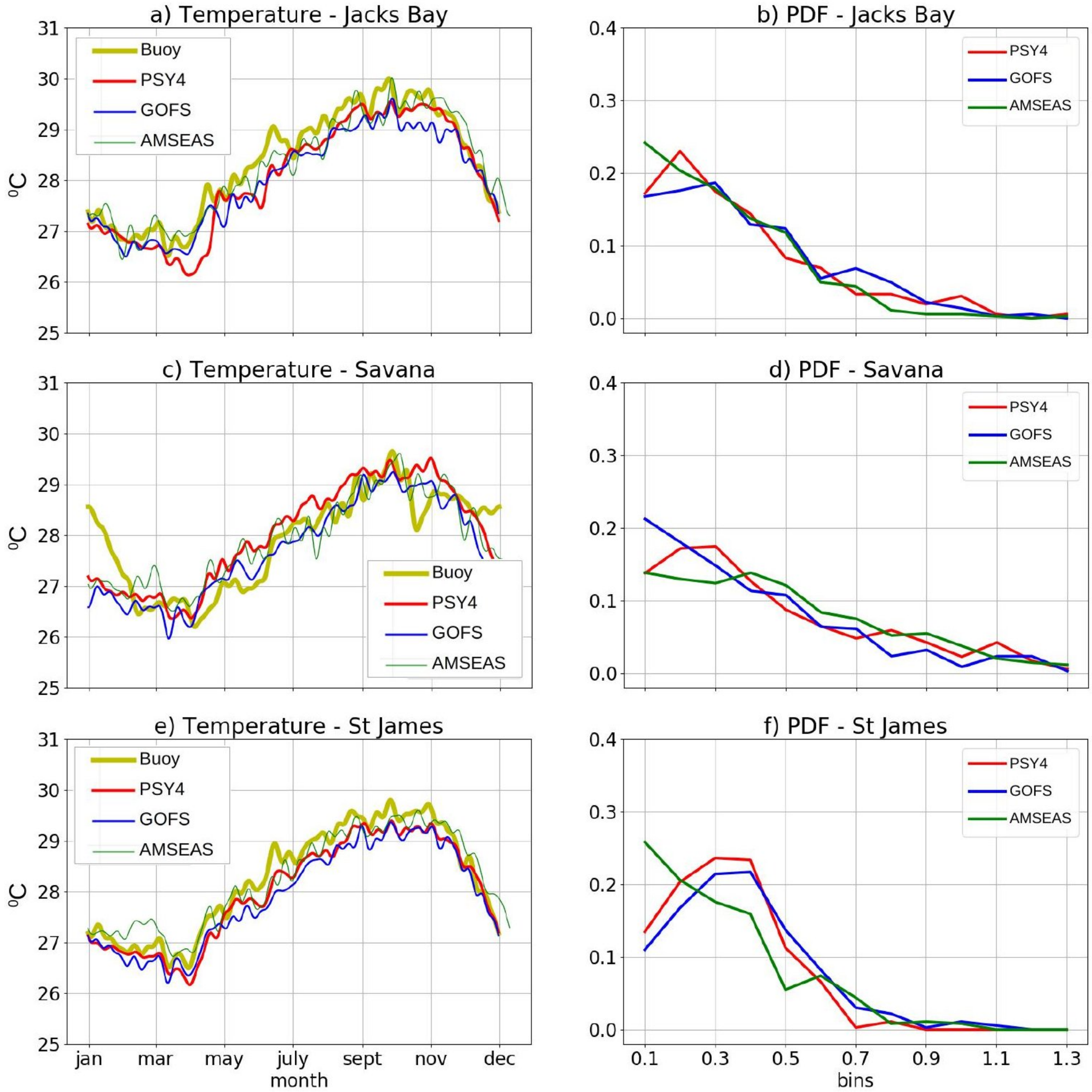

Figure 16: Seasonal variability of the benthic temperature (left panel) measured by HOBO loggers at the coral reef sites at Jacks Bay (13 m depth), Savana (16 m depth) and St James (27 m depth) in 2016, and the model outputs at the same locations. The right panel shows the PDF of the corresponding model errors. Refer to section 5.3 for details on the PDF calculation.